Circumnuclear Structures in Megamaser Host Galaxies

Patryk Pjanka[1], Jenny E. Greene[1], Anil C. Seth[2], James A. Braatz[3], Christian Henkel[4,5], Fred K. Y. Lo[3], and Ronald Läsker[6]

[1] Department of Astrophysical Sciences, Princeton University, 4 Ivy Lane, Princeton, NJ 08544, USA; ppjanka@princeton.edu
[2] Department of Physics and Astronomy, University of Utah, Salt Lake City, UT 84112, USA
[3] National Radio Astronomy Observatory, 520 Edgemont Road, Charlottesville, VA 22903, USA
[4] Max-Planck-Institut für Radioastronomie, Auf dem Hügel 69, D-53121 Bonn, Germany
[5] Astronomy Department, King Abdulaziz University, P.O. Box 80203, Jeddah 21589, Saudi Arabia
[6] Finnish Centre for Astronomy with ESO (FINCA), University of Turku, Väisäläntie 20, FI-21500 Kaarina, Finland
Received 2017 January 9; revised 2017 May 26; accepted 2017 June 25; published 2017 August 3

Abstract

Using the *Hubble Space Telescope*, we identify circumnuclear (100–500 pc scale) structures in nine new H_2O megamaser host galaxies to understand the flow of matter from kpc-scale galactic structures down to the supermassive black holes (SMBHs) at galactic centers. We double the sample analyzed in a similar way by Greene et al. and consider the properties of the combined sample of 18 sources. We find that disk-like structure is virtually ubiquitous when we can resolve <200 pc scales, in support of the notion that non-axisymmetries on these scales are a necessary condition for SMBH fueling. We perform an analysis of the orientation of our identified nuclear regions and compare it with the orientation of megamaser disks and the kpc-scale disks of the hosts. We find marginal evidence that the disk-like nuclear structures show increasing misalignment from the kpc-scale host galaxy disk as the scale of the structure decreases. In turn, we find that the orientation of both the ∼100 pc scale nuclear structures and their host galaxy large-scale disks is consistent with random with respect to the orientation of their respective megamaser disks.

Key words: galaxies: nuclei – galaxies: structure – ISM: kinematics and dynamics – masers

1. Introduction

It is now commonly accepted that supermassive black holes with masses of 10^5–10^{10} $M_\odot$ (SMBHs) ubiquitously reside in galactic centers (Rees 1984, Kormendy & Ho 2013). The evidence of their existence extends to redshifts of ∼7 (Mortlock et al. 2011; Venemans et al. 2013; De Rosa et al. 2014). How such massive black holes can form only ∼0.8 Gyr after the Big Bang is still a mystery.

One of the main mechanisms proposed to fuel SMBHs is the inflow of cold gas from the large-scale galaxy (Heckman et al. 1978). The final accretion itself is obviously facilitated on extremely small scales, where the infalling material radiates as an active galactic nucleus (AGN). However, for the gas to travel from the kpc-scale galaxy to the outer accretion structures at ≲1 pc, more than four orders of magnitude in angular momentum must be lost. The details of this angular momentum extraction process are not yet fully understood.

On galaxy-wide scales, there are several potential mechanisms responsible for dissipation of angular momentum. Secular interactions between a (collisionless) stellar component and (collisional) gas in non-axisymmetric kpc-scale galactic structures (such as bars or spiral arms) can drive gas inward (e.g., Hopkins & Quataert 2010), and these interactions may be triggered in a variety of ways. During gas-rich mergers, tidal forces destabilize galactic disks to form non-axisymmetries, as seen by the numerical experiments of Hernquist (1989), Barnes & Hernquist (1996), Hernquist & Mihos (1995), and others. Observational results confirm that mergers accompany nuclear activity in some sources (Canalizo & Stockton 2001; Ellison et al. 2011), but there is growing evidence that mergers are not the main kpc-scale driving mechanism of AGN activity, at least at moderate luminosity (Cisternas et al. 2011; Ellison et al. 2011; Kocevski et al. 2012; Villforth et al. 2014). The driver of kpc-scale galactic gas inflow likely depends on AGN

luminosity and redshift (Hopkins & Hernquist 2009; Treister et al. 2012; Comerford & Greene 2014). Transient interactions between galaxies, or non-axisymmetric gravitational instabilities in isolated disk galaxies (Cavaliere & Vittorini 2000; Hopkins & Quataert 2010; Gatti et al. 2015), can also drive gas inflows. At high redshift, torques may be supplied by massive star-forming regions in gas-rich galaxies; such "clumps" are most frequently seen at redshift of ∼2 (Shibuya et al. 2016), and models suggest that they sink in the gravitational potential of their host, driving gas inflow (Noguchi 1998; Bournaud et al. 2007; Genzel et al. 2008).

However, torques induced by large-scale structures cannot efficiently extract angular momentum at distances <1 kpc from the galactic center (Goodman 2003). Viscosity-related effects are not efficient enough beyond the last parsec from the black hole (Shlosman & Begelman 1989; Goodman 2003). Gravitational torques may again be a viable solution. The "bars within bars" model, originally proposed by Shlosman et al. (1989), assumes the presence of a series of embedded bars, stretching all the way from kpc scales to the central SMBH accretion structures. These structures are expected to gradually remove angular momentum from the gas, letting it reach the galactic center sufficiently fast to explain AGN activity. The "bars within bars" mechanism, later revised to the "non-axisymmetric features all the way down" model (also referred to as the "stuff within stuff" model) to account for non-axisymmetries other than bars (Hopkins & Quataert 2010, 2011), has been found to arise in close to self-consistent nested zoom-in simulations of Hopkins & Quataert (2010, 2011) and tested in several high-resolution numerical studies (Escala 2007; Anglés-Alcázar et al. 2017). Moreover, central ∼100 pc scale dust structures with various morphologies have been observed in a number of active and inactive galaxies (Jungwiert et al. 1997; Regan & Mulchaey 1999; Márquez et al. 2000; Martini et al. 2003), and their morphologies confirm the viability of

gravitational instabilities as the main gas inflow mechanism at ∼100 pc scales (Maiolino et al. 2000; Davies et al. 2009, 2014; Haan et al. 2009; Combes et al. 2014).

If the "non-axisymmetric features all the way down" model is true, how do its features manifest in observations? One general feature is theoretically predicted by Hopkins et al. (2012). They report that the non-axisymmetric structures are expected to progressively misalign from the disk of their host galaxies as they reach further into the galaxy. Here we search directly for these structures on ∼100 pc scales using *Hubble Space Telescope* (*HST*) data, for a special sample of AGN where we know the orientation of the accretion disk precisely.

An especially precise measurement of the orientation of the central accretion flow in galactic nuclei is possible with observations of H_2O megamasers (see Greene et al. 2013 and a review by Lo 2005). The maser emission in these systems originates in a ring of material illuminated by the AGN at a distance of ∼0.1–0.5 pc from the black hole. The ring is located in the viscous-torque-dominated region of gas inflow and is thus expected to align with the accretion disk around the black hole. These megamaser disks are only detected when they are close to edge-on, since in that orientation the optical depth for maser action is maximized. Mapping with VLBI at sub-pc resolution (e.g., Greenhill et al. 1990; Kuo et al. 2011, see also Lo 2005) provides a very precise three-dimensional orientation for the accretion disk, a great advantage over other methods. Combined with *HST*/WFC3 images of the host galaxy, these properties make them excellent targets for investigation of how the orientation of nuclear non-axisymmetries correlates with the orientation of the SMBH's accretion disk. Such a comparison, along with the morphological characterization of identified nuclear structures, is the main goal of this work.

The paper is organized as follows. In Section 2 we describe the instruments and technical details of the observations, as well as initial data reduction leading to the results presented in the following sections. In Section 3, the methods of identification and classification of the nuclear regions are presented. Calculations related to the orientation of galactic structures based on optical images are described in Section 3.5. Our results concerning the morphologies of nuclear regions are given in Section 4, and the relative orientation of various components within our galaxies is presented in Section 5. We discuss and summarize our findings in Section 6. In Appendix A we present detailed information on our analysis of each of the 9 new megamaser galaxies. In Appendix B we consider how the morphological classification of the nuclear regions in our sample depends on galaxy distance, scale of the region, and available resolution.

2. Observations and Data Reduction

There are 34 known megamaser disk galaxies (Pesce et al. 2015). We focus here on a subset of 18 megamaser disk galaxies, with reliable BH mass measurements from Keplerian fitting to the maser dynamics (Kuo et al. 2011; Gao et al. 2016, 2017 and W. Zhao et al. 2017, in preparation). The list of our sources is given in Table 1. In general, the galaxies are early-type spiral galaxies (e.g., Greene et al. 2010), and we have studied the detailed morphological structure of roughly half of the galaxies in Läsker et al. (2016) using the *HST*.

Each target was observed in two orbits with *HST* between 2014 December 1 and 2015 August 29. We obtained F336W,

F438W, F814W, F110W, and F160W (roughly UBIJH) images of each galaxy with integration times of 1320, 430, 2140, 150, and 420 s, respectively. In the optical, we use a three-point dither pattern for cosmic-ray removal, and in the NIR we use the four-point dither pattern. We use the default output of the MultiDrizzle pipeline, which performs cosmic-ray rejection and optimally combines the images.

3. Data Analysis

The goal of this paper is to characterize the innermost structures in galaxies with maser disks. Here we describe the classification of these structures and the process of deriving their orientation from *HST* data.

3.1. Ellipse Fitting

In order to support the identification of nuclear structures in our sample of galaxies, we used the algorithm of Jedrzejewski (1987) to fit ellipses to the galaxy isophotes, implemented as the IRAF script ellipse.[7]

The initial analysis was performed using IRAF. First the foreground stars and background galaxies were manually masked (in DS9[8]). The centers of the galaxies in NIR- and UVIS-band filters were found using the task imexamine and fed to an ellipse parameter file as initial ellipse center positions. The ellipse centers were then further refined by ellipse. In some cases (all filters for Mrk 1029, F336W for ESO 558 and J0437+2345, F438W for UGC 3193, as well as F336W and F438W for NGC 5765b), the "object locator's k-sigma threshold" was also lowered from the default value of 1.0 to 0.5 in order for the algorithm to correctly identify the galactic center.

For each of our targets, the ellipse run conducted as noted resulted in a list of elliptical fits to image isophotes for each of the filters; we use the parameters of those fits in further analysis.

3.2. Structure Maps

As a second method to characterize nuclear morphology, we use structure maps to remove large-scale smooth galaxy components and highlight the small-scale features (such as dust lanes). The concept of structure maps was introduced by Pogge & Martini (2002). The technique is designed to remove low-frequency (smooth) features of the map, and highlight high-frequency features around the scale of the PSF. The method is closely related to Richardson–Lucy deconvolution (Richardson 1972; Lucy 1974). It is also similar in spirit to unsharp masking, but with structure maps, the convolution is done with the PSF itself rather than a boxcar. Mathematically, a structure image is given by Equation (1) of Pogge & Martini (2002):

$$S = \left[\frac{I}{I \otimes P} \right] \otimes P^T, \qquad (1)$$

where S is the structure image pixel matrix, I is the original image, P is the point-spread function (PSF), P^T is the transposed PSF, and $\otimes$ denotes convolution. Structure maps

---

[7] The ellipse is included in STSDAS (version 3.17), available as a package for IRAF (version 2.16.1 used).
[8] SAOImage DS9, http://ds9.si.edu.

Table 1
Orientation of the Masing Disk, Galaxy, and Nuclear Region for Each of the Galaxies

(1)	Object (2)	D_A (Mpc) (3)	Maser i (4)	Maser PA (5)	Maser ref. (6)	Galaxy e (7)	Galaxy i (8)	Galaxy PA (9)	Nuclear Region Class (10)	Nuclear Region r (pc) (11)	Nuclear Region e (12)	Nuclear Region i (13)	Nuclear Region PA (14)
This work	ESO558−G009	109	90	350	G16p†	0.97	104	277[d]	Ch+N	210	0.87	61	99
	J0437+2456	70	90	115	G16p†	0.82	125	126[d]	Bu+N	120	0.77	51	131
	Mrk1029	117	90	300	G16p†	0.77	130	176[d]	D + N	220	0.83	57	126
	Mrk1210	58	101	333	Z17p	0.33	19	36[r]	D/R+Stw	170	0.45	26	119
	NGC5495	93	90	270	G16p†	0.63	141	119, 299	D/R+Sgd	170	0.49	29	57
	NGC5728	41	90	329	K17p†	0.91	114	302[r]	R+Stw	460	0.36	21	121
	NGC5765b	126	95	237	G16	0.67	42	337[r]	R+Stw	450	0.45	27	67
	UGC3193	60	90	60	W17p†	0.95	72	80[d]	D?+N	220	0.90	65	79
	UGC 6093	147	94	70	Z17p	0.47	152	0[r]	Bu?+N	150	0.26	15	92
Greene et al. (2013)	IC2560	44	90	44	Y12	0.88	62	133[r]	D+Stw	100	0.74	48	136
	NGC1194	52	85	67	K11	0.84	57	50[r]	Ch+N	120	0.63	39	68
	NGC2273	26	84	63	K11	0.68	43	176[r]	R+Stw	150	0.86	59	131
	NGC2960	71	89	139	K11	0.64	140	314[r]	D+N	260	0.83	56	139
	NGC3393	55	90	56	K08†	0.72	46	252[r]	R+Sgd	270	0.68	43	58
	NGC4388	19	90	17	K11†	0.98	78	0	D+N	100	1.00	89	345
	NGC6264	134	90	185	K11	0.79	52	290[d]	Ch+N	290	0.68	43	123
	NGC6323	103	89	280	K11	0.94	70	85[r]	Bu?+N	200	0.62	38	95
	UGC3789	45	89	311	K11	0.87	120	243[r]	D+Sgd	100	0.62	39	88

Note. Column 1—data sample. Column 2—galaxy designation. Column 3—angular diameter distance from NED (http://ned.ipac.caltech.edu/; with its default cosmology: $H_0 = 73$ km s^{-1} Mpc^{-1}, $\Omega_m = 0.27$, $\Omega_\Lambda = 0.73$) or using data from Gao et al. (2016) in the case of NGC 5765b. Columns 4–6—inclination (i) and position angle (PA) of the maser disk as reported in reference in column 6. Hereafter $i < 90°$ corresponds to a feature whose angular momentum is directed toward Earth and $i > 90°$ corresponds to a feature whose angular momentum is directed away from it. References with † do not constrain inclination, and $i = 90°$ is assumed there. Columns 7–9—large-scale galaxy orientation. e denotes the average eccentricity of `ellipse` fits identified as following the orientation of the galaxy as a whole (see Section 3.3). Note that eccentricity e is given by ellipticity ϵ through $e = \sqrt{1 - (1 - \epsilon)^2}$. i and PA are the inclination and position angle resulting from e, PA$_{avg}$, rotation curves of the galaxies (superscript "r"; see Schommer et al. 1988; Cooke et al. 2000; Schulz & Henkel 2003; Fischer et al. 2013; van den Bosch et al. 2015) or the relative prominence of their dust lanes (superscript "d"; see Section 3.5), and the assumption that the spiral arms of all the galaxies are trailing. For NGC 4388, instead of `ellipse` fits, kinematic arguments from Greene et al. (2014) are used to constrain the nuclear disk and galaxy orientation. Columns 10–14—nuclear region orientation based on the smallest scales at which such measurement is possible with our data. Column 10—morphological class (see Section 3.4). Classes of the nuclear region: D—disk, R—ring, Bu—bulge, B—bar, Ch—no discernible morphology. Classes of the nuclear spiral: N—no surrounding spiral dust structure, Sx—spiral structure visible, where x denotes its type ("gd"—two-arm grand-design, "tw"—tightly wound or flocculent). Column 11—outer physical radius of the nuclear region (disk assumed). e—average eccentricity of ellipse fits identified as following the orientation of the nuclear region. i—smaller of the two possible inclinations allowed by e. PA—smaller of the two possible position angles allowed by the data.

References. G16—Gao et al. (2016), G16p—Gao et al. (2017), K08—Kondratko et al. (2008), K11—Kuo et al. (2011), K17p—C.-Y. Kuo et al. (2017, in preparation), W17p—J. Wagner et al. (2017, in preparation), Y12—Yamauchi et al. (2012), Z17p—W. Zhao et al. (2017, in preparation).

emphasize high-frequency features that are nearly unresolved in the original image.

In our analysis we used structure maps to highlight dust features in the galaxies of our sample. Two filters in our data set, F438W and F814W, are suitably sensitive to dust to derive the structure maps from them. F438W provides higher spatial resolution and is more sensitive to dust. However, in our data, the F814W filter has significantly better signal-to-noise ratio than F438W. In our analysis we have therefore used the structure maps based on the F814W images.

The structure map derivation proceeded as follows. We extracted a sky-subtracted and re-centered PSF from each of the images. A lower cutoff n_0 for the count rate per pixel of 0.00001 was set, and all the pixels on both the original F814W image and the PSF with count rates $n < n_0$ were assigned count rates n_0 in order to avoid division by zero and negative values. Each of the F814W images was then convolved with its respective PSF obtained in previous steps.[9] Finally, a copy of

the original image was divided by the result of the previous step, and the resulting image was convolved with a transposed PSF template. The structure maps for all the new sources can be found in Figures 1 and Appendix A.

The re-analysis of the sources of Greene et al. (2013) was performed analogously.

3.3. Identifying Nuclear Structures

We consider a range of scales in this work: the 0.1–0.5 pc scale of the megamaser disk, the nuclear scales of 100–500 pc where we seek kinematically cold or flattened structures ("nuclear regions") along with spiral features ("nuclear spirals"), and the galaxy-wide disk on kpc scales.

Many galaxies are known to have nuclear disks on 10–100 pc scales (e.g., Combes et al. 2014; García-Burillo et al. 2014), and we resolve the 100 pc scales in 10 of our 18 galaxies. With the theoretical resolution limits of the F110W ($\sim$1153.4 nm), F160W ($\sim$1536.9 nm), and F814W ($\sim$802.4nm) filters being 0.12, 0.16 and 0.08 arcsec, respectively, we identify nuclear structures at least 0.3 arcsec in size (which limits the visibility of 100 pc structures to $\sim$70 Mpc; see Table 1 for distances to the galaxies in our sample). The outer

---

[9] For Mrk 1210 and UGC 6093, the PSFs obtained using point sources in their F814W images were strongly asymmetric, resulting in dipole-like artifacts visible on the structure maps. Therefore we decided to use a more stable PSF from NGC 5495 in calculation of the structure maps in these two cases.
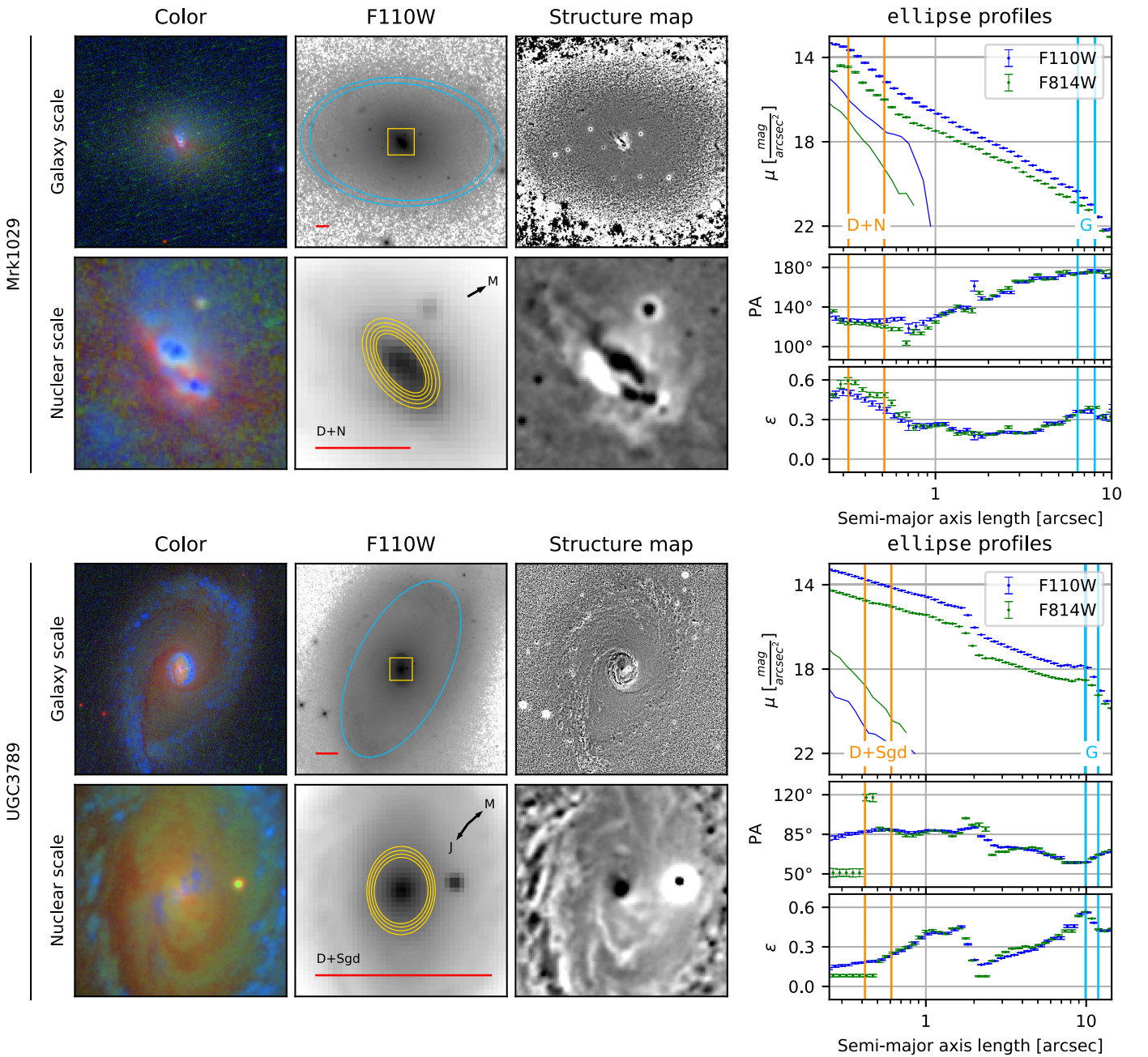
Figure 1. Images and `ellipse` fits of two of the galaxies in our sample (for analogous figures for the remaining eight of the nine new galaxies, see Appendix A; UGC 3789 was taken from the Greene et al. 2013 sample). In all images, north is up and east is left. Each row shows images of the same field of view (top in each panel—galaxy scales, bottom—nuclear scales). Column 1 (from left to right): false-color images (blue—F335W, green—F438W, and red—F814W). Column 2: F110W image (color—logarithmic scale for count rate). Column 3: structure maps constructed from the F814W image (logarithmic scale). In the F110W image in the top row (second column), ellipses following the galaxy-wide orientation are marked in blue, and a yellow rectangle shows the region presented in the bottom row. In the F110W image in the bottom row, ellipses tracing the nuclear region are marked in yellow. The PA of the maser disk angular momentum vector, perpendicular to the line of nodes of the masing disk, and the PA of the jet (if known) are shown in the upper right corner of this image as black arrows marked with "M" and "J," respectively. Jet orientation references for all sources where such data were available include (see Appendix A) Schommer et al. (1988), Falcke et al. (1998), Schmitt et al. (2001), Mundell et al. (2009), Xanthopoulos et al. (2010), Yamauchi et al. (2012), Sun et al. (2013), and the FIRST survey, Becker et al. (1994). The red bar at the bottom of each F110W image is 1 kpc in projected distance. Nuclear class (see Section 3.4) is noted above the red bar on the nuclear-scale image. Column 4: Surface brightness (μ, blue and green circles with horizontal bars indicating the angular range), position angle (PA), and ellipticity (ϵ) profiles from `ellipse` for the F110W (blue) and F814W (green) images. Note that eccentricity $e = \sqrt{1 - (1 - \epsilon)^2}$. Vertical blue and orange lines limit the ranges of ellipse major axes used to extract the orientation of a galaxy as a whole and the nuclear region, respectively. The type of each structure is indicated. Blue and green solid lines on the surface brightness plots show `ellipse` fits to point sources in F110W and F814W images, respectively, approximating the point-spread function (PSF). The PSF profiles have been artificially scaled in brightness to optimize their visibility on the plots.

radii of our nuclear regions range between 0.3 and 2.3 arcsec, with a median of 0.6 arcsec. In most cases we operate at the very limits of what can be robustly resolved and identified. However, we sometimes select larger structures that have a clearer interpretation to be able to analyze morphology and/or

be better equipped to extract the orientation of the nuclear regions.

To ensure that the lower limit of the nuclear region's angular size of 0.3 arcsec is sufficient, we have re-derived all the results presented in Sections 4 and 5, adopting a more restrictive limit

Table 2
Relative Orientation of Structures

(1)	Object (2)	Galaxy—inner region		Galaxy—maser		Inner region—maser	
		ΔPA (degree) (3)	3D angle (degree) (4)	ΔPA (degree) (5)	3D angle (degree) (6)	ΔPA (degree) (7)	3D angle (degree) (8)
This work	ESO558−G009	2, 178	15, 43, 137, 165	73	74	71, 109	73, 107
	J0437+2456	…	…	11	36	…	…
	Mrk1029	50, 130	40, 86, 94, 140	124	115	6, 174	33, 147
	Mrk1210	83, 97	30, 34, 146, 150	63	92	34, 146	58, 79, 101, 122
	NGC5495	62, 118	35, 58, 122, 145	29, 151	57, 123	33, 147	66, 114
	NGC5728	1, 179	45, 87, 93, 135	27	36	28, 152	72, 108
	NGC5765b	90	49, 131	100	100	10, 170	58, 68, 112, 122
	UGC 3193	1, 179	7, 43, 137, 173	20	27	19, 161	31, 149
	UGC 6093	…	…	70	77	…	…
Greene et al. (2013)	IC2560	3, 177	14, 70, 110, 166	89	89	88, 92	89, 91
	NGC1194	18, 162	22, 85, 95, 158	17	32	1, 179	46, 56, 124, 134
	NGC2273	45, 135	38, 88, 92, 142	113	101	68, 112	68, 75, 105, 112
	NGC2960	5, 175	16, 84, 96, 164	175	131	0, 180	33, 35, 145, 147
	NGC3393	14, 166	10, 88, 92, 170	164	134	2, 178	47, 133
	NGC4388	15	19	17	21	32	32
	NGC6264	13, 167	13, 86, 94, 167	105	102	62, 118	71, 109
	NGC6323	…	…	165	154	…	…
	UGC 3789	25, 155	28, 84, 96, 152	68	72	43, 137	62, 63, 117, 118

Note. Column 1—data sample. Column 2—host galaxy name. Columns 3–4—projected position angle difference (ΔPA) and 3D angle between the angular momenta of the galaxy as a whole and the nuclear region. Columns 5–8—orientation of the maser disk relative to the galaxy as a whole (columns 5–6) and the nuclear region (7–8). In each case, all the angles allowed by the data are given (see the discussion on degeneracy of relative orientation angles in Section 3.5).

on the angular size of a nuclear region of 0.5 arcsec (i.e., excluding eight galaxies that host nuclear regions with radii <0.5 arcsec from the analysis). This corresponded to removing most of the galaxies beyond 100 Mpc from the sample. Our conclusions (see Sections 4 and 5) remained mostly unchanged. For specific results of this trial and their discussion, see Appendix B.2.

With `ellipse` fits and structure maps in hand, we proceed to identify nuclear structures in our sample galaxies. While we took into account all the available filters, we concentrated our efforts on F110W (or F160W) and F814W (the deepest image in the UVIS band), with F110W tracking starlight and F814W−F110W interstellar dust. For each of our galaxies, we have chosen a set of ellipses that we associate with the large-scale galaxy, assuming that the isophotes on large scales are fit by an axisymmetric disk. These define the "kpc-scale" galaxy to which we refer in the following sections. We also identify a set of ellipses associated with the outer edge of a nuclear structure of size ∼50–600 pc. We carefully pick those isophotes to correspond to changes in PA and ellipticity profiles, so that they correspond to a physical feature in the galactic nucleus (for details on how the structures are identified, see Section 3.4).

3.4. Classification of Nuclear Structure

To discuss the morphology of nuclear structures, we classify them in two ways. First, we assign a class to the region itself, according to the key:

- D—disk,
- R—ring,
- Bu—bulge,

- B—bar,
- Ch—no discernible morphology, chaotic dust structure.

An additional "?" sign marks class assignment as unsure.

Nuclear spirals are almost ubiquitously found in late-type spiral galaxies (e.g., Pogge & Martini 2002; Martini et al. 2003). We therefore add a classification of potential spiral dust structure surrounding our set of nuclear isophotes, which we append to the nuclear region classification after a "+" sign:

- N—no surrounding spiral dust structure;
- Sx—spiral structure visible, where x denotes its type ("gd"—two-arm grand-design, "tw"—tightly wound or flocculent).

For example, class D/R+Stw is assigned to a galaxy with a central disk or ring with a tightly wound spiral structure—as in the case of Mrk 1210 (see Figure 9 and Table 1).

The outputs from `ellipse` aid our identification of nuclear structures in the following manner (cf. Greene et al. 2013):

- Bars are characterized by a region of constant position angle (PA), ellipticity (ϵ) decreasing inwards, and rapid ϵ and PA changes at their outer edge (Maciejewski et al. 2002; Erwin & Sparke 2003)—see, for example, the ∼4″-scale bar in UGC 6093, Figure 14.
- Spiral structure is identified by smoothly rotating PA with ϵ constant or changing (Martini et al. 2003)—see the spiral structure outside 5″ in UGC 6093, Figure 14.
- Disks can be recognized by relatively constant PA and significant ellipticity—see the nuclear disk at ∼0″.6 in Mrk 1210, Figure 9.
- Rings exhibit features similar to disks, but are distinguished by discontinuities in PA at their edges, as well as

Table 3
Results of the KS Tests

Species		Angle	Limit	N	KS-stat	p-value
(1)	(2)	(3)	(4)	(5)	(6)	(7)
Gal	Nuc	ΔPA	30°	15	0.33	0.05
Gal	Nuc	ΔPA	90°	15	0.40	0.01
Gal	Nuc(S)	ΔPA	30°	7	0.43	0.11
Gal	Nuc(S)	ΔPA	90°	7	0.29	0.50
Gal	Nuc(L)	ΔPA	30°	8	0.33	0.27
Gal	Nuc(L)	ΔPA	90°	8	0.59	3×10^{-3}
Nuc	Mas	ΔPA	90°	15	0.29	0.13
Nuc(S)	Mas	ΔPA	90°	7	0.24	0.83
Nuc(L)	Mas	ΔPA	90°	8	0.44	0.06
Nuc	Mas	3D	90°	15	0.23	0.37
Nuc(S)	Mas	3D	90°	7	0.25	0.70
Nuc(L)	Mas	3D	90°	8	0.29	0.42
Gal*	Mas	ΔPA	90°	18	0.23	0.24
Gal*	Mas	3D	180°	17	0.20	0.46

Note. The results of one-sample KS tests as described in Section 5.1. Columns 1–2: structures in the galaxy whose angular momenta orientations are being compared. Gal—angular momentum of the galaxy as a whole, Gal*—the same limited to galaxies with orientation fixed using rotation curves or the relative dust lane prominence method, Nuc—the nuclear regions (in some cases divided into S—those with $r < 200$ pc and L—with $r \geqslant 200$ pc), Mas—the megamaser disk. Column 3: type of relative angle: ΔPA is the position angle difference (as defined in the text), 3D denotes the 3D angles between angular momenta. Column 4: upper limit of the range of the respective angle in which the control distribution is random (the lower limit in all cases is 0). Column 5—number of sources in the sample. Columns 6–7—KS-statistic (column 6; maximal difference between CDFs, or cumulative distribution functions, of the sample and test distribution) and p-values (column 7; likelihoods of the sample being drawn from the test distribution) resulting from each of the tests.

"bumps" in the surface brightness profiles (Buta 1986)—see $\sim 2''$ nuclear ring of NGC 5728, Figure 11.

- While the ellipse results should show bulges as round (i.e., with low ellipticity), with constant PA, and a surface brightness profile that is steadily rising toward the center (see, e.g., the $\sim 3''$-scale bulge in UGC 3193, Figure 13), confident classification of bulges requires detailed 2D modelling of a galaxy (see, e.g., Läsker et al. 2016); we do not attempt such decomposition here, and therefore nuclear regions classified as bulges in this work should be treated as tentative.

These considerations are only one part of our analysis. We also consider color and structure maps. For example, flocculent or tightly wound nuclear spirals are best detectable with structure maps, which improve the visibility of any PSF-scale structure, regardless of its symmetry, while they would fall below the spatial resolution of ellipse profiles. In turn, if narrow line regions (NLRs) are present in a galaxy image, they are best distinguished from dust structures by color maps, on which they appear very blue. The NLR emission may hide any dust components in the structure map, but the contamination due to the NLR can be visible in a color image (see the conical structure in NGC 5728, Figure 11, which we interpret following Schommer et al. 1988 and Wilson et al. 1993 as an AGN ionization cone). Finally, the F110W data traces stellar light, and allows us to distinguish features corresponding to the stellar component of galactic nuclei, enabling us to verify whether a circular feature visible in the galaxy image may correspond to a bulge.

In some parts of our analysis, it is beneficial to divide the nuclear regions in our sample into smaller and larger regions. The radius separating these two groups, $r_b = 200$ pc, provides an equal number of objects in each size bin: there are nine small nuclear regions ($r < 200$ pc) and nine large nuclear regions ($r \geqslant 200$ pc); see Table 1. We admit that the 200 pc boundary is somewhat arbitrary, but small changes in this value that roughly keep sample sizes similar do not yield different results of our analysis. As noted in Section 3.3, all of our nuclear structures were identified at sizes of at least 0.3 arcsec. While re-deriving all the results presented in Sections 4 and 5 with a more restrictive limit on angular size of a nuclear region of 0.5 arcsec (see Section 3.3 and Appendix B.2), we also made sure that the determination of orientation for small ($r_b < 200$ pc) nuclear regions is not affected by resolution effects. In the restricted sample, the differences between large and small nuclear regions are still apparent, and the sample is still evenly divided at 200 pc—for specific results, see Appendix B.2.

3.5. Angular Momentum Orientation from Ellipse Fits

If a nuclear region is disk- or ring-like, the orientation of its angular momentum in space is easily recovered from the ellipse fits. For each source, we calculate the positions of the angular momenta of the galaxy as a whole and the nuclear region, utilizing the groups of ellipses described in Section 3.3. We take the average PA and eccentricity ($e = \sqrt{1 - (1 - \epsilon)^2}$) within the region and calculate $i = \arccos(\sqrt{1 - e_{\mathrm{avg}}^2})$. Note that the PA we quote is for the angular momentum vector and is thus aligned with the minor axis of the projected disk. For instance, PA = 30° describes a disk with its projected angular momentum pointing 30° from north toward east on the sky, and the image of the nuclear region in this case appears elongated along the PA = 120° direction, with the blueshifted edge in the direction of PA = 120° and the redshifted edge in the direction of PA = 300°. Four possible three-dimensional angular momentum directions are allowed by $\mathrm{PA_{avg}}$ and i. The PA can be $\mathrm{PA_{avg}}$ or $\mathrm{PA_{avg}} + 180°$, and an inclination of either i or $180° - i$ is allowed (where $i = 0$ corresponds to the angular momentum of the disk pointing toward the Earth). We are *assuming* that the nuclear region is a disk (treated as infinitely thin) to make this assignment. We quantify the accuracy of such an assumption by assigning a class to each nuclear region (see Section 3.4). The nuclear bulges are ignored in our analysis of nuclear regions' orientations, as their orientation cannot be established using the method described here. We do, however, consider the three nuclear regions with chaotic dust structures in our sample to correspond to flattened structures, and take their orientations into account.

There are important biases associated with our estimation of 3D positions of angular momenta, especially for nuclear regions. If a nuclear region is edge-on, the ellipse will still fit a finite-width ellipse to its isophotes due to vertical structure in the disk and finite PSF, giving $i \neq 0$ (the floor appears to be $i_{\min} \sim 20°$; see Table 1). We also avoid face-on nuclear regions due to random structure in the plane of the disk distorting
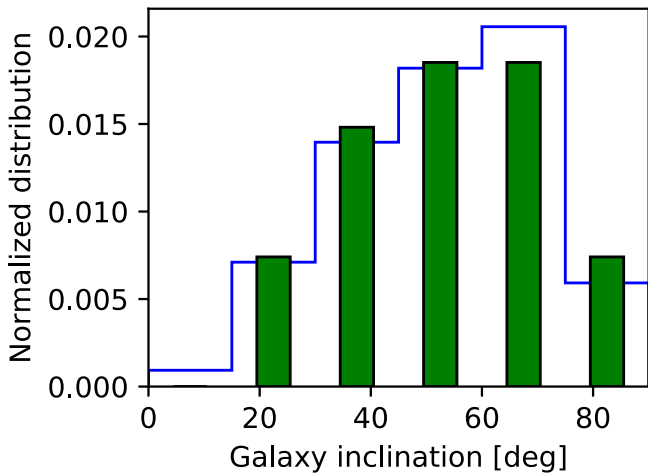
Figure 2. Comparison of galaxy inclinations in our sample with SDSS data, histograms are normalized so that the sum of all bins in each series multiplied by the width of the bins (15° in both cases) is equal to 1. The inclination distribution of 788 disk galaxies from SDSS DR4 (Nair & Abraham 2010; see Section 5.1.1 for details of galaxy choice from their sample) is shown as the blue curve. For the sake of the comparison presented here, we ignore the information about spiral arms in our galaxies and present the lower of two possible inclination angles allowed in such case (see main text for discussion) as narrow green bars. In all other analyses in this work, the unambiguous galaxy inclination angle in [0°, 180°] range is used.

`ellipse` fits and potential misclassification of face-on disks as bulges.

In the case of the set of ellipses associated with the kpc-scale disk, additional information can be used to further constrain the orientation of the angular momentum. All of the galaxies in our sample are spirals. If we assume that the spiral arms are trailing, as is observed in most spiral galaxies (see Binney & Tremaine 2008 and references therein), this fixes the inclination and leaves only two possible orientations. In some cases, the rotation curves of the galaxies are also available, leaving only one angular momentum orientation allowed by the data.

For the galaxies without rotation curves available, we have used the relative prominence of dust lanes in the galaxy to constrain the orientation, a method originally suggested by Hubble (1929) and used by, for example, Sharp & Keel (1985) and Väisänen et al. (2008). The dust lanes of the part of the galaxy in front of its nucleus as seen by the observer are expected to be more pronounced than those behind it, due to their being back-lit by stronger galactic emission closer to the nucleus. The only galaxy where a rotation curve is not available and dust lanes prominence method does not yield a reliable orientation (due to the galaxy being almost face-on) is NGC 5495, where we have kept both possible PAs of the angular momentum in the analysis. Table 1 gives all the resulting PA and inclination values for each of the galaxies.

In our investigations, we also use results and expand the analysis of Greene et al. (2013) in order to derive the statistics of the total sample of 18 sources. The data related to these galaxies are included in the summary in Table 1.

4. Results: Morphology of Nuclear Regions

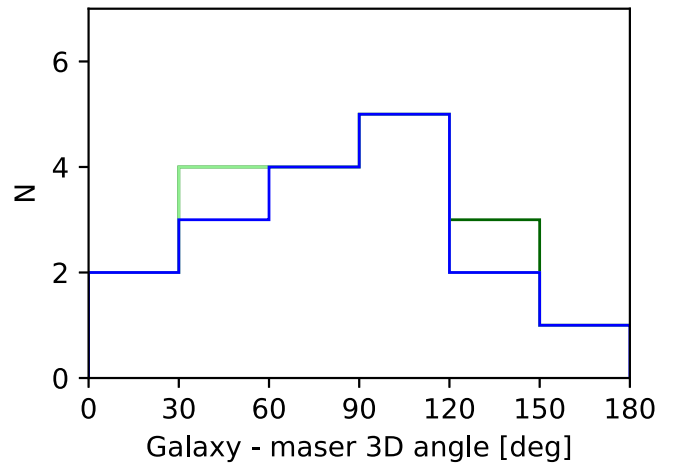Figures 1 and Appendix A show the ellipses corresponding to the large-scale galaxy and the nuclear region.

Figure 3. Galaxy-maser orientation comparison, 3D angle (angle between angular momenta of the two regions). The blue curve shows the histogram for sources with known rotation curves or orientation fixed using the relative dust lane prominence method. The light and dark green curves correspond to the addition of the two possible 3D angles for NGC 5495. The distribution is consistent with random (see text; Section 5.1.1).

When it comes to the nuclear regions, our sample of 18 galaxies contains 12 disky structures, four of which are rings, two of which are disk/ring structures, and six of which do not exhibit any additional morphology. We also identify three bulges and three chaotic dust structures. There are three sources with grand-design nuclear spirals and five with tightly wound ones. Two of the former belong to galaxies with a large-scale bar (the exception being UGC 3789), while all of the latter belong to non-barred galaxies. Ten galaxies do not show any nuclear spirals associated with the identified regions.

4.1. Comparison with Previous Work

We see a significant amount of structure in the galactic nuclei, consistent with the predictions of the "non-axisymmetric features all the way down" model and previous studies of nuclear dust structures in active galaxies (Xilouris & Papadakis 2002; Simões Lopes et al. 2007; Hicks et al. 2013). Throughout, we assume that the megamaser disk galaxies are a fair sample of spiral galaxies, but in principle we do not know this, and must bear in mind the caveat that the masers may be a special subset of all spiral galaxies (see, e.g., Greene et al. 2016).

Martini et al. (2003) performed a detailed characterization of nuclear spirals in their matched galaxy samples (28 pairs of active/inactive galaxies and 18 pairs of barred/unbarred ones). As we conduct a similar morphological classification here, it is worthwhile to compare our results with theirs. Martini et al. (2003) report the presence of nuclear spirals for 75% of their 28 active galaxies. In our sample this fraction is considerably lower: 8 out of 18 galaxies (i.e., 44%). The results are, however, marginally consistent with each other if nominal uncertainties in each sample of ~16% are taken into account.

All of our tightly wound (tw) nuclear spirals belong to galaxies lacking a large-scale bar, in agreement with the results of Martini et al. (2003). It is intriguing to note that one of our three grand-design nuclear spirals, in UGC 3789, also appears to lack a large-scale bar. While Martini et al. (2003) and other early works (Englmaier & Shlosman 2000; Martini 2004)
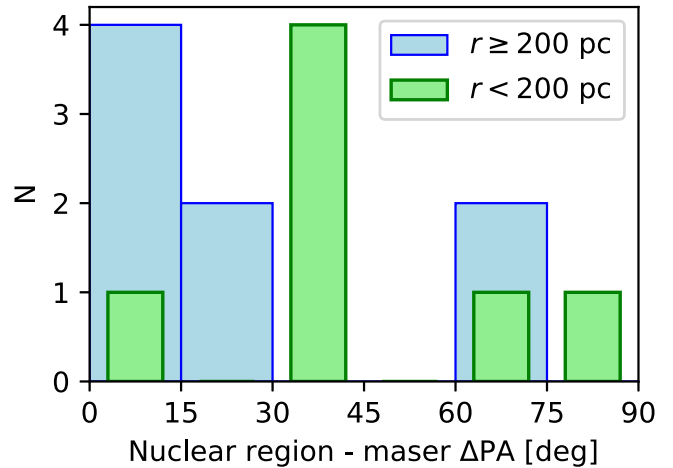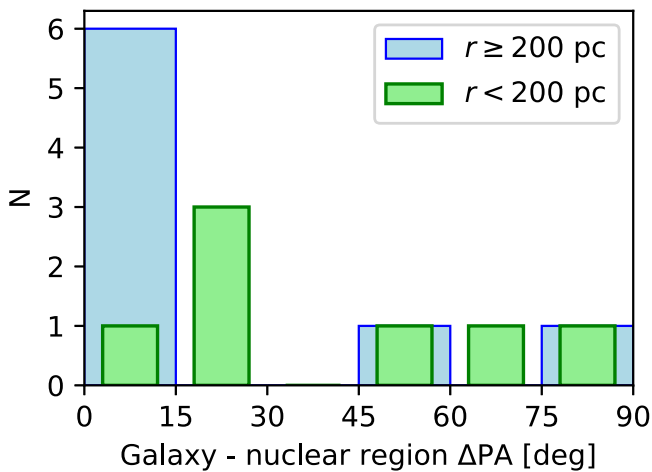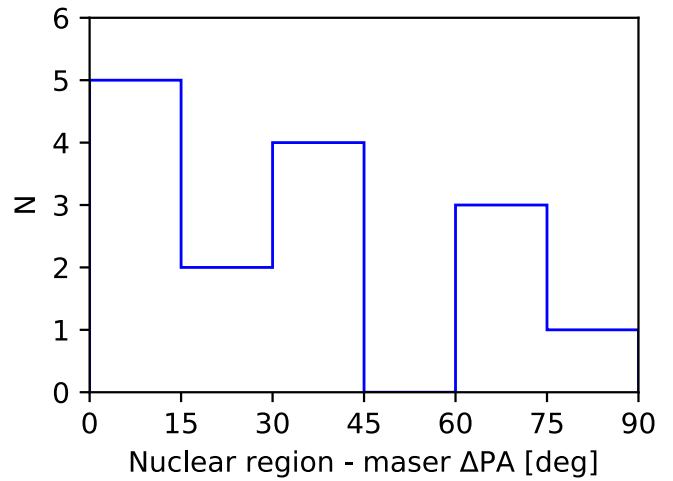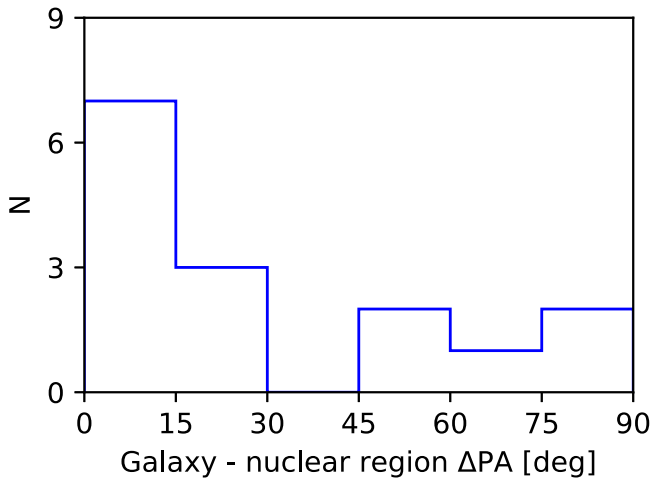
Figure 4. Position angle difference between the angular momenta of the galaxy and its nuclear region. Only the smaller of two possible angles is shown (the other one is the result of subtraction of the shown angle from 180°). Top: full sample. Bottom: small ($r < 200$ pc) and large ($r \geqslant 200$ pc) nuclear regions shown separately as (narrow) green and (full-width) blue bars. The observed misalignment arises due to the smaller nuclear regions (see text, Section 5.1.2).

Figure 5. Position angle difference between nuclear region and maser angular momentum orientation. Only the smaller of two possible angles is shown (the other one is the result of subtraction of the shown angle from 180°). Top: full sample. Bottom: small ($r < 200$ pc) and large ($r \geqslant 200$ pc) nuclear regions shown separately as (narrow) green and (full-width) blue bars. Both small and large nuclear regions are consistent with being randomly oriented with regard to their megamaser disks (see text, Section 5.1.3).

argued that grand-design nuclear spirals are associated mostly with strongly barred galaxies, our findings are fully consistent with later works (e.g., Peeples & Martini 2006 and Kim et al. 2012), who find no evidence of such a correlation on the smallest scales. Kim et al. (2012) also predict that grand-design nuclear spirals should preferentially occur with circular (x_2-type) kpc-scale rings—such a ring is indeed seen in UGC 3789. The galaxy also contains a pair of rings in an 8-shaped structure at scales of ~20 kpc. Their presence suggests that the grand-design nuclear behavior may have been caused by a recent merger. We note, however, that such ring structures are not necessarily a result of interactions and may also arise from the intrinsic dynamics of this galaxy (Kormendy & Kennicutt 2004). The fraction of tightly wound spirals in our sample (5 out of 18 galaxies; i.e., ~28%) is consistent with that reported by Simões Lopes et al. (2007), who find them in ≲25% of their samples of early-type (elliptical and lenticular) galaxies. Whether nuclear dust morphology depends on galaxy type is, so far, uncertain

(Xilouris & Papadakis 2002; Martini et al. 2003; Simões Lopes et al. 2007).

5. Results: Angular Momenta

Table 1 gives the orientation of the angular momentum of the galactic masers, nuclear regions, and kpc-scale disks, with the latter two based on the `ellipse` fits shown in Figures 1 and Appendix A. Note that nuclear bulges are excluded from this analysis.

5.1. Relative Orientation of Angular Momenta

The 3D angles and projected PA differences between the angular momenta of different subcomponents in our analysis are given in Table 2.

To quantify the trends visible in the relative orientation of the angular momenta in our samples, we use one-sample Kolmogorov–Smirnov (KS) tests. This common statistical test
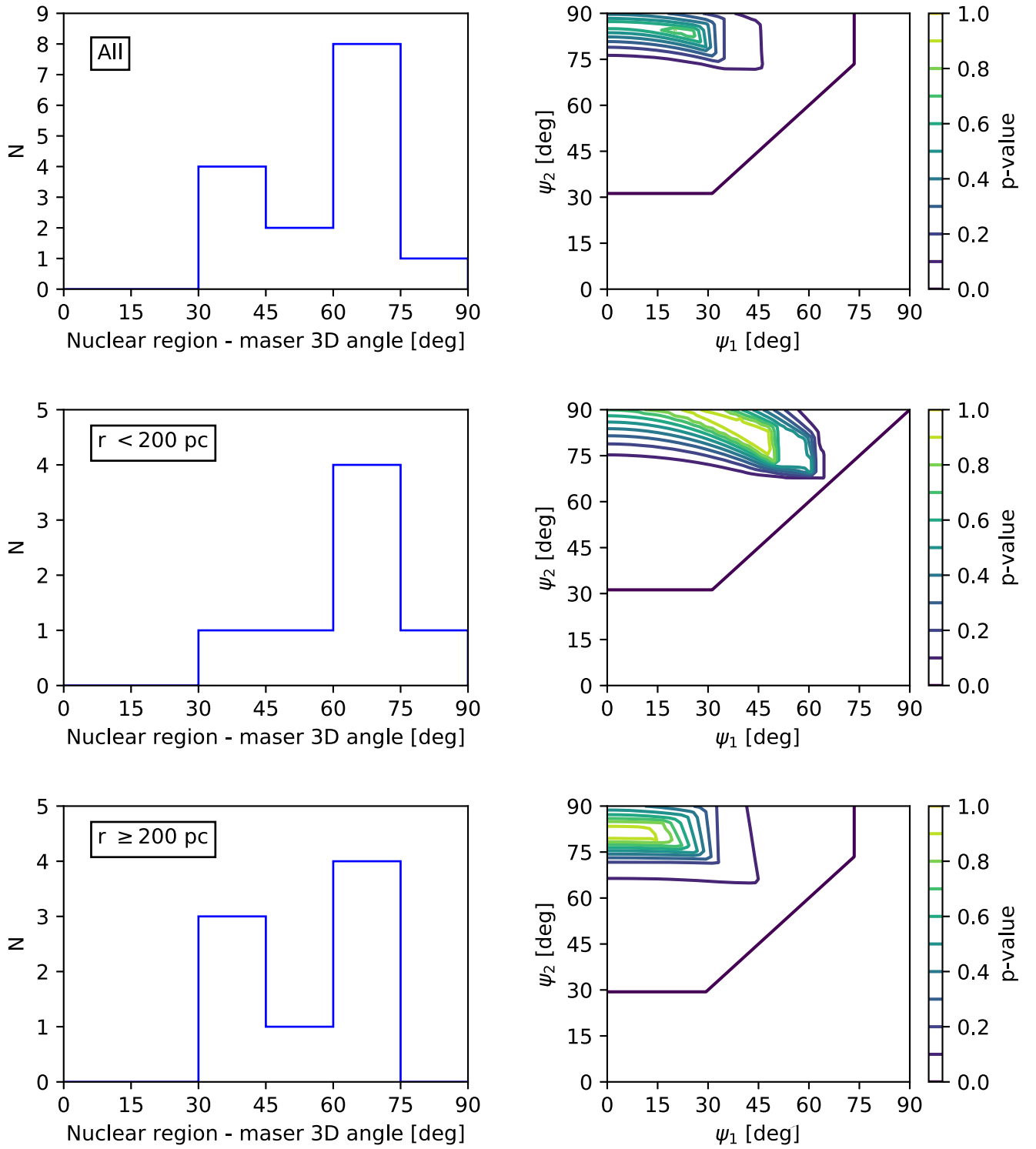
Figure 6. Left: histograms of 3D angles between angular momentum orientation of the nuclear region and the masing disk for all sources (top), nuclear regions smaller than 200 pc (middle), and those larger than 200 pc (bottom). Only the lower half of the full distribution ($\psi \in [0, 180°]$) is shown, limiting the data to the lower of two possible 3D angles (see main text for discussion). Right: contour maps of p-values obtained by comparison of respective samples with random distribution of 3D angles between ψ_1 and ψ_2 by means of one-sample KS tests. The regions of highest p-value (light green) in the right column correspond to the regions in parameter space favored by the data. The distribution is consistent with random ($\psi_1 = 0$, $\psi_2 = 90°$) for both small and large nuclear regions (see text, Section 5.1.3).

allows us to assess whether a given sample is drawn from a specified distribution.

In our implementation, we use KS tests to assess whether the relative orientation of the angular momenta between two subcomponents (e.g., the maser disk and galaxy as a whole) could have been drawn from a random distribution between some limiting values. In the case of 3D angles ψ, the randomly distributed sample has a distribution $\frac{dN}{d\psi} \propto \sin(\psi)$. The

cumulative distribution function (CDF) of such a distribution with $\psi \in [\psi_1, \psi_2]$ is given by

$$\mathrm{CDF}_{3D}(\psi) = \begin{cases} 0, & \psi < \psi_1; \\ \dfrac{\cos\psi_1 - \cos\psi}{\cos\psi_1 - \cos\psi_2}, & \psi_1 < \psi < \psi_2; \\ 1, & \psi_2 < \psi. \end{cases} \quad (2)$$

For the projected PA differences between vectors, the random distribution is flat. The CDF of such a distribution with $\mathrm{PA} \in [\mathrm{PA}_1, \mathrm{PA}_2]$ is simply

$$\mathrm{CDF}_{\Delta PA}(\mathrm{PA}) = \begin{cases} 0, & \mathrm{PA} < \mathrm{PA}_1; \\ \dfrac{\mathrm{PA} - \mathrm{PA}_1}{\mathrm{PA}_2 - \mathrm{PA}_1}, & \mathrm{PA}_1 < \mathrm{PA} < \mathrm{PA}_2; \\ 1, & \mathrm{PA}_2 < \mathrm{PA}. \end{cases} \quad (3)$$

The KS-statistics and p-values resulting from comparisons of these CDFs with CDFs of respective data samples are given in Sections 5.1.1–5.1.3, where applicable, and summarized in Table 3.

5.1.1. Masing Disks Are Randomly Oriented Relative to kpc-scale Disks

Let us start with the largest scales in our analysis, the orientation of the galaxy on kpc scales (columns 7–9 in Table 1). We first compare inclinations of our galaxies with those reported for disk galaxies by Braatz et al. (1997) and the Sloan Digital Sky Survey Data Release 4 (SDSS DR4). For our sample of 18 galaxies, the assumption of trailing spiral arms allows us to place each galaxy's inclination within the full [0°, 180°] range (0° meaning that the angular momentum pointing toward Earth and 180° meaning the angular momentum pointing away from it). Since inclinations reported in Braatz et al. (1997) and SDSS DR4 are based on ellipticity only, each of them allows two possible angular momentum orientations for the galaxy: for each i_{lit}, $180° - i_{\mathrm{lit}}$ is also possible (see discussion in Section 3.5). For the sake of the comparison presented here, we ignore the information about spiral arms winding directions in our galaxies and consider the lower of two possible inclination angles allowed in such case. In all other analyses in this work, the unambiguous galaxy inclination angle in the [0°, 180°] range is used.

From a comparison of our results shown in Figure 2 with Figure 9 of Braatz et al. (1997), we can see that the maser galaxies in our sample appear to follow the inclination distribution of the entire population of galaxies—both with and without detected megamasers. We check this result by performing a two-sample KS test with a sample of 788 disk galaxies from SDSS DR4, using the galaxy morphology classification of Nair & Abraham (2010). From their sample of 14,034 galaxies (limited to redshifts of $0.01 < z < 0.1$ and g'-band magnitudes brighter than 16 mag), we have chosen reliably classified (T-Type flag = 0) galaxies of types Sa-Sd (T-Type of 1–7) and without signs of interaction (interaction flag "2'" in their notation). The two-sample KS test of these 788 sources with our data results in a KS-statistic (maximal difference between CDFs of the two samples) of 0.12 and p-value (likelihood of the two samples being drawn from the same distribution) of 0.94. The inclinations of our galaxies are then strongly representative of the entire population of disk galaxies.

Thus the orientation of the maser disk is unlikely to depend on the orientation of the host galaxy.

Such a non-correlation excludes the possibility that the gas inflow within the central pc is associated with non-axisymmetries in the large-scale structure of the galaxy. As this result is further supported by the considerations listed later, we discuss it in more detail in Sections 5.1.3 and 6.

We also directly compare the kpc-scale structures with the orientation of the maser disks. Figure 3 shows the histograms describing the relative orientation of the galaxy as a whole and the maser disk. In the case of the 3D angles for the galaxies with orientation fixed by rotation curves or relative prominence of dust lanes (blue curve), the distribution is consistent with being random: for the 3D angles between $\psi_1 = 0$ and $\psi_2 = 180°$, KS-statistic $\simeq 0.20$ and p-val $\simeq 0.46$.

5.1.2. Large Nuclear Regions Align with kpc-scale Galaxy while Small-sized Ones Are Oriented Randomly

We next compare the orientation of the kpc-scale galaxy with the 100 pc scale nuclear regions. Overall, the nuclear regions have too broad a distribution of projected ΔPA to be aligned; the p-value for comparison with a fully random distribution is only 0.01 (see Figure 4 and Table 3). There seems to be a weak hint of misalignment growing with the decreasing scale of the structure. If we cut our random control distribution at a maximum angle of $\Delta \mathrm{PA}_2 = 30°$, we see that the large nuclear regions are consistent with this aligned sample, while for smaller nuclear regions, a fully random distribution is much more likely (see Table 3). While this division is arbitrary, the difference suggests that the nuclear structure progressively misaligns from the large-scale disk. We caution, however, that the evidence for this behavior is marginal.

While the boundary between smaller and larger nuclear regions of 200 pc, on which the numerical results presented previously are based, is somewhat arbitrary (see Section 3.4), there is a clear change toward more misalignment as the structure size approaches <100 pc scales.

We then observe a build-up of misalignment with regard to the large-scale galactic disk as we go deeper into the galactic nucleus. If this misalignment continues to grow, once we reach ~0.1 pc scales, at which megamaser disks reside, the gaseous disk is completely randomly oriented with regard to the galactic disk (see the next subsection).

5.1.3. Nuclear Regions Are Randomly Oriented with Regard to the Megamaser Disks

Now we compare the 100 pc scale nuclear regions with objects on the smallest scales in our analysis—the maser disks ~0.5 pc from the SMBH. Figure 5 shows the difference in projected PA (ΔPA) between the angular momenta of the nuclear region and the maser disk. For the entire sample, the ΔPA distribution is consistent with being random, and the K-statistic and p-value give (0.29, 0.13). Then, the left column of Figure 6 shows the distribution of 3D angles between the angular momenta of the nuclear region and the maser disk. Note that due to the maser disk being edge-on, only two such angles result from the data.[10] The two possible angles are symmetric with respect to 90° (i.e., for each 3D angle ψ,

---

[10] In the cases where the inclination of the maser disk is known to be different from 90°, the resulting 3D angle possibilities consist of two pairs of close angles (see Table 2). In these cases, averages of those pairs are used here as the two possible 3D angles.
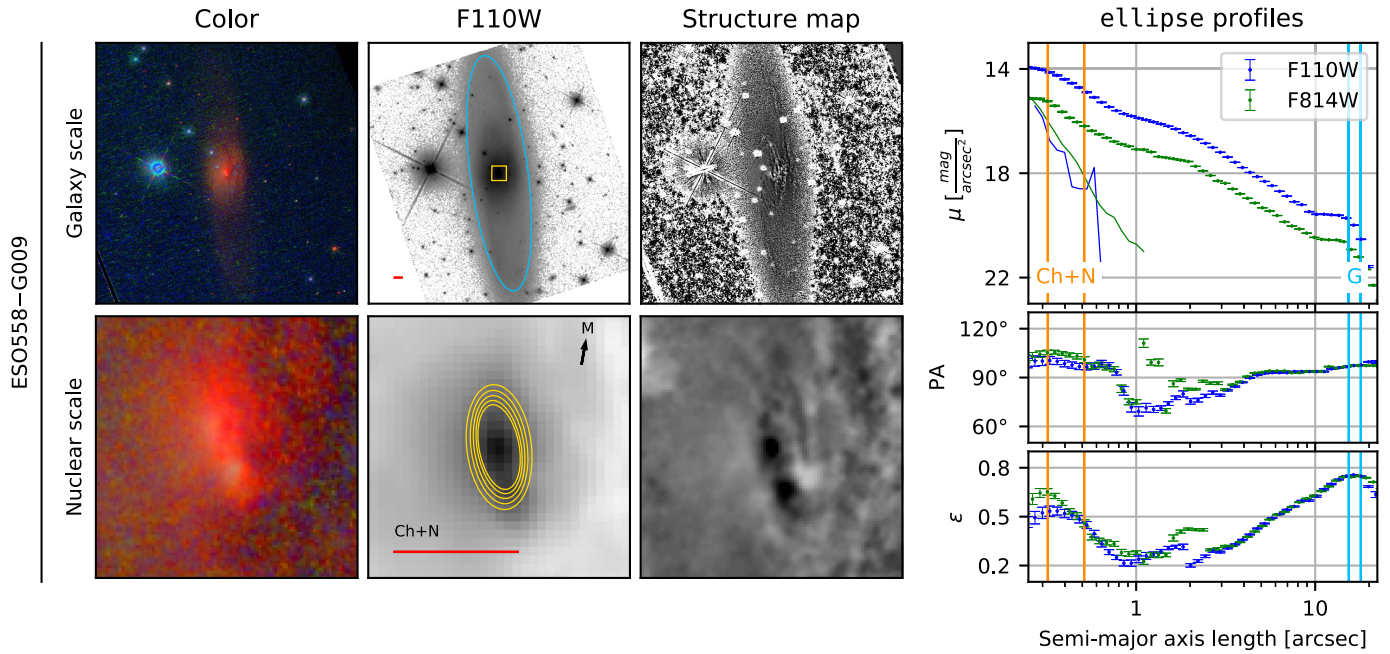
Figure 7. Images and `ellipse` fits of ESO 558−G009. The order of images and plots, as well as the meaning of symbols and designations, are the same as in Figure 1. In all images, north is up and east is left. Column 1 (from left to right): false-color images (blue—F335W, green—F438W, and red—F814W). Column 2: F110W image (color—logarithmic scale for count rate). Column 3: structure maps constructed from the F814W image (logarithmic scale). In the F110W image in the top row (second column), ellipses following the galaxy-wide orientation are marked in blue, and a yellow rectangle shows the region presented in the bottom row. In the F110W image in the bottom row, ellipses tracing the nuclear region are marked in yellow. The position angle of the maser disk angular momentum vector, perpendicular to the line of nodes of the masing disk, and the PA of the jet (if known) are shown in the upper right corner of this image as black arrows marked with "M" and "J," respectively. Jet orientation references for all 18 sources (where presented): Schommer et al. (1988), Falcke et al. (1998), Schmitt et al. (2001), Mundell et al. (2009), Xanthopoulos et al. (2010), Yamauchi et al. (2012), Sun et al. (2013), and the FIRST survey, Becker et al. (1994). The red bar at the bottom of each F110W image is 1 kpc in projected distance. Nuclear class (see Section 3.4) is noted above the red bar on the nuclear-scale image. Column 4: Surface brightness (μ, blue and green circles with horizontal bars indicating the angular range), position angle (PA), and ellipticity (ϵ) profiles from `ellipse` for the F110W (blue) and F814W (green) images. Note that eccentricity $e = \sqrt{1 - (1 - \epsilon)^2}$. Vertical blue and orange lines limit the ranges of ellipse major axes used to extract the orientation of a galaxy as a whole and the nuclear region, respectively. The type of each structure is indicated. Blue and green solid lines on the surface brightness plot show `ellipse` fits to point sources in F110W and F814W images, respectively, approximating the point-spread function (PSF). The PSF profiles have been artificially scaled in brightness to optimize their visibility on the plots.

$180° - \psi$ is also possible.[11] Since the two possible angles are symmetric with respect to 90°, we only take into account the smaller of them and compare the resulting distribution with a random distribution of 3D angles between ψ_1 and ψ_2. This is equivalent to assuming that the true distribution is also symmetric with respect to 90° and comparing only its lower half to a random distribution. Alternatively, we also tried to use both angles as two separate measurements (resulting in a measured distribution symmetric with respect to 90°), but the results were then highly dependent on our assumption of symmetry with respect to 90°, and thus less informative of the observed distribution.

Contour plots of p-values resulting from comparison of a random distribution between 3D angles ψ_1 and ψ_2 with the distribution of the smaller of the possible 3D angles between nuclear regions and their respective masers are shown in Figure 6. The distributions for the entire sample, as well as small and large nuclear regions separately, are consistent with random orientations: the KS-statistic and p-value pairs for $\psi_1 = 0$ and $\psi_2 = 90°$ are (0.23, 0.37) for the entire sample, (0.25, 0.70) for the small, and (0.29, 0.42) for the large nuclear regions. While the lower limit seems to be preferred at $\psi_1 > 0$,

we attribute this to our distributions being biased away from $\psi_1 = 0$ (see Section 3.5). Alternatively, an asymmetric distribution of true 3D angles $\{\psi_i\}$ would cause our distribution $\{\min(\psi_i, 180° - \psi_i)\}$ to be inconsistent with random, even if all nuclear regions do orient randomly with respect to their megamasing disks up to an angle of $\psi_2 \gtrsim 90°$.

Our data fully support the hypothesis that the orientation of nuclear regions in our sample is not correlated with the orientation of the maser disks, regardless of the size of the nuclear region. This agrees well with previous results concerning the relative orientation of these structures that were obtained using jet orientation (Ulvestad & Wilson 1984; Nagar & Wilson 1999; Kinney et al. 2000; Schmitt et al. 2002; Gallimore et al. 2006), reflection spectroscopy (Middleton et al. 2016), narrow emission-line regions (Fischer et al. 2013), and previous results drawn from H_2O megamaser orientations (Greene et al. 2013). In the framework of the "non-axisymmetric features all the way down" model, this would mean that the non-axisymmetries responsible for the final infall of gas to the central supermassive black holes (expected to be aligned with the central accretion disk) are still unresolved in our observations.

This result augments and adds to the findings of Martini et al. (2003). Using *HST* data, they found that the type of nuclear spiral at ∼100 pc does not correlate with AGN activity (see also Simões Lopes et al. 2007). They conclude that the 100 pc scales do not determine the accretion state of the

---
[11] For the purpose of this part of our analysis, we ignore the fact that for NGC 4388 the orientation of the inner nuclear region is fixed by Greene et al. (2014) and instead assume that also there two 3D angles are possible: 58° (the true result) and 180°–58°. This allows us to analyze the entire sample in a homogeneous manner.
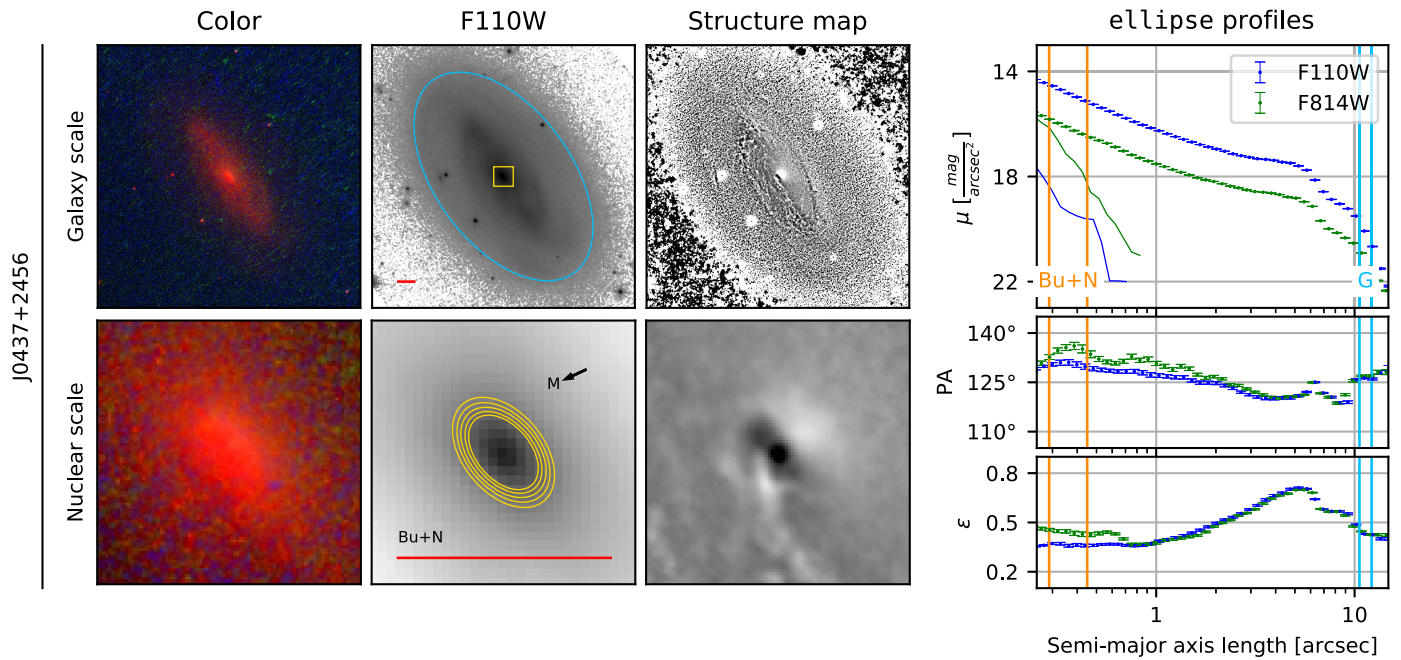
Figure 8. Images and `ellipse` fits of J0437+2456. The order of images and plots, as well as the meaning of symbols and designations, are the same as in Figure 1.

galactic nucleus. This finding allowed them to constrain the duty cycle of AGN activity, requiring the duration of the active phases to be shorter than a few Myr (the typical dynamical time at 100 pc). In addition, inflows have been observed to be associated with non-axisymmetries at these scales in observations using integral field spectroscopy (IFS; Davies et al. 2009; Riffel et al. 2013; Diniz et al. 2015, and references therein).

The emerging picture is that while gas inflow feeding the SMBH passes through the ∼100 pc scales, the on/off state of AGN accretion is regulated closer to the galactic center. With this in mind, some signs of galactic nuclear activity are visible in the dynamical state of gas at 100 pc scales. There are hints that active galaxies have more centrally concentrated and more rotationally dominated central regions (<200 pc; Hicks et al. 2013), as well as a possibly higher molecular gas content within similar scales (Izumi et al. 2016).

The nature of the on/off switch of galactic activity may be relevant to AGN feedback considerations. Currently, the numerical experiments regarding this process rarely resolve structures below 100 pc and usually use more finely resolved simulations at smaller scales (such as those of Hopkins et al. 2012) to generate prescriptions regulating the nuclear activity. If the true dynamics of SMBH feeding deviates from these prescriptions, the large-scale AGN feedback simulations may overestimate the overall accretion rate, and thus the total feedback. Precise timing of AGN on/off states may also be relevant to AGN feedback. However, this latter dependence may be non-trivial, and its details are beyond the scope of this work.

6. Discussion and Summary

We investigate nine new megamaser host galaxies, doubling the sample of Greene et al. (2013). We use *HST*/WFC3 data to identify the innermost resolved structures in each of them. In order to select those regions and extract their orientations, we use the ellipse-fitting algorithm of Jedrzejewski (1987) and structure maps of Pogge & Martini (2002). We compare the

orientation of each 100–500 pc scale nuclear region with the orientation of its host galaxy and the megamaser disk. We conclude:

1. The orientation of the galaxy relative to the masing disk is random—confirming the separation of large-scale structure from the central gas infall onto the SMBH.
2. The nuclear regions likely become increasingly misaligned from the large-scale galactic disk as their scale decreases. The ones smaller than 200 pc are likely completely misaligned from the kpc-scale galaxy. There is a hint that larger nuclear regions are more aligned, as they show a preference for a maximum (arbitrarily chosen) 3D angle of 30° over that of a fully random distribution.
3. The orientation of the nuclear region relative to the masing disk is consistent with random, regardless of the size of the region; we conclude that ∼100 pc scale structures still do not directly couple to the inner accretion flow responsible for AGN activity, in agreement with previous studies.

We find that the structures within a galaxy become more and more misaligned as we approach the central supermassive black hole. While nuclear regions larger than 200 pc in radius appear to align with their kpc-scale disk, the smaller ones become completely randomly oriented with respect to the large-scale structure. The central ∼0.1 pc scale maser disk appears randomly oriented relative to both the nuclear regions and the kpc-scale galaxy. We therefore confirm the results of previous studies that both large-scale structures (Kinney et al. 2000; Gallimore et al. 2006; Middleton et al. 2016) and those at ∼100 pc scales (Schmitt et al. 2002; Martini et al. 2003) do not couple directly to the central accretion flow. We conclude that the mechanism driving the final gas inflow onto the SMBH must operate closer to the black hole itself. Our findings are in agreement with the "non-axisymmetric features all the way down" model, where the nuclear structures are expected to increasingly misalign from the large-scale disks of galaxies as
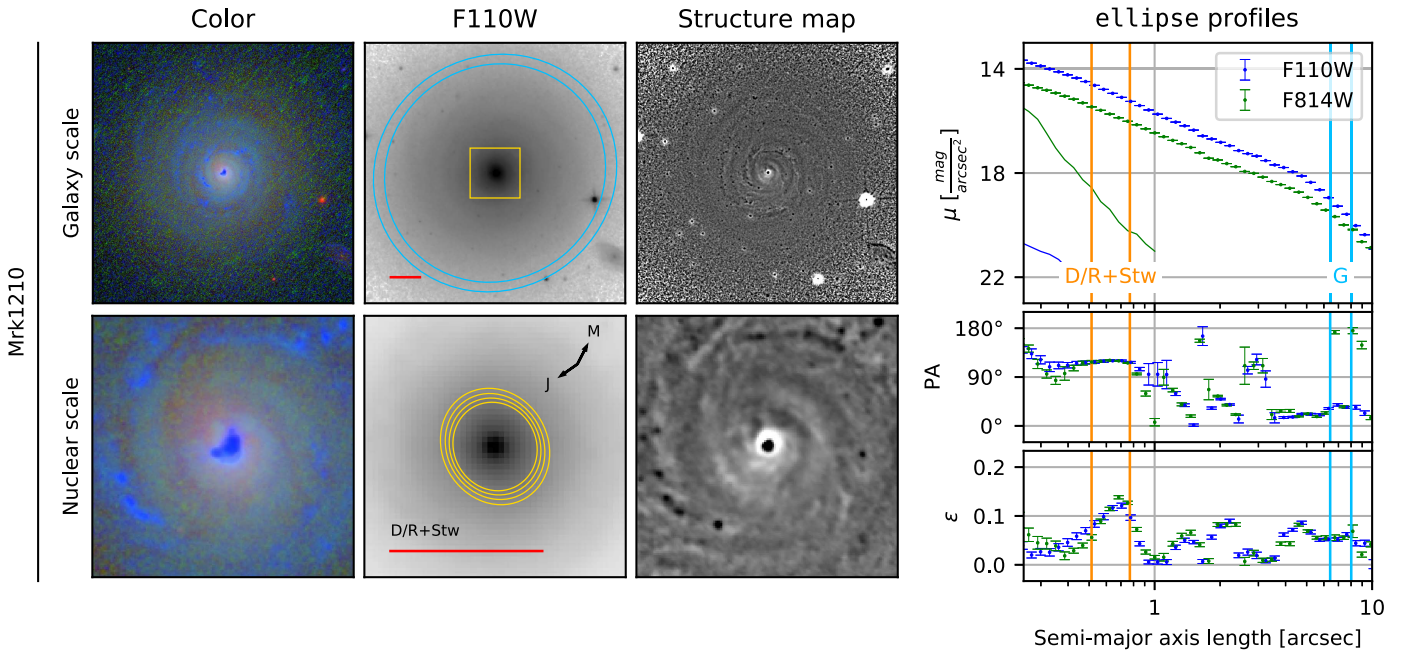
Figure 9. Images and `ellipse` fits of Mrk 1210. The order of images and plots, as well as the meaning of symbols and designations, are the same as in Figure 1.

they transport gas farther and farther in (Hopkins et al. 2012). In the final parsec, where the gas reaches the megamaser disk and the AGN accretion disk, the flow may become completely misaligned from even the intermediate-scale structures.

We favor a picture in which accretion is contingent on torques leading to shifts in angular momentum that randomize the orientations that we observe, but there are alternative explanations. One is that the gas on small scales has an external origin (e.g., Bertola et al. 1984; Morganti et al. 2006). However, as mergers do not appear to be common enough to explain all nuclear activity (Cisternas et al. 2011; Kocevski et al. 2012), this alternative cannot apply to all Seyfert galaxies. Very likely inflows mediated by both gravitational instability and galaxy interactions occur some of the time, as argued by Sarzi et al. (2006) for the case of lenticular and elliptical galaxies. In the case of the megamaser disk galaxies considered here, NGC 2960 is a likely merger remnant (Läsker et al. 2016), and NGC 5765b is a member of an interacting pair of galaxies (Gao et al. 2016). UGC 3789 contains a pair of rings in an 8-shaped structure, but they are not necessarily a result of interactions and may arise from the intrinsic dynamics of this galaxy (Kormendy & Kennicutt 2004). Another possible channel of gas inflow comes from numerous interactions with small galaxies. However, as no galaxies other than NGC 2960 and NGC 5765b in our sample show obvious signs of recent disturbance (Gao et al. 2016; Läsker et al. 2016), this does not appear to be at work in the galaxies considered here.

Warping of the nuclear galactic disk due to radiation pressure supplied by the AGN (Maloney et al. 1996; Pringle 1997; Gammie et al. 2000) is also worth consideration. At megamaser scales, these processes result in warps observed in radio imaging of the maser spots (e.g., Neufeld & Maloney 1995; Greenhill et al. 2003; Herrnstein et al. 2005). This sub-parsec-scale deformations could misalign the observed masing disk direction with regard to the nuclear disk at 100 pc scales, where the gas is unaffected by warping due to AGN radiation pressure.

We identify nuclear spirals in 8 out of 18 galaxies in our sample. One of them (UGC 3789) appears to be grand-design and resides in a galaxy without a large-scale bar, which has not been expected based on previous studies. We confirm that the tightly wound nuclear spirals preferentially reside in non-barred galaxies.

While megamaser host galaxies are an excellent target for an analysis of SMBH feeding mechanisms, the sample of such sources with optical imaging of sufficient angular resolution is very limited. As of now, only ∼20 megamaser hosts have been imaged with *HST* (Greene et al. 2010, this work). There are 34 H_2O megamaser disks currently known (Pesce et al. 2015; van den Bosch et al. 2016), so this number may double in the near future as additional observations are made. Moreover, upcoming instruments like the Atacama Large Millimeter/submillimeter Array and the *James Webb Space Telescope* will allow to image the thermal gas at the galactic centers of megamaser host galaxies with unprecedented resolution and/or spectral capabilities. Using these data, which would directly trace the gas, our analysis could be repeated on a more statistically significant sample of sources. For now, however, our work presents the state of the art of optical imaging of megamaser host galactic nuclei—we hope that not only will it broaden the understanding of gas inflows in galactic nuclei, but it will also be a useful starting point for similar endeavors in the future.
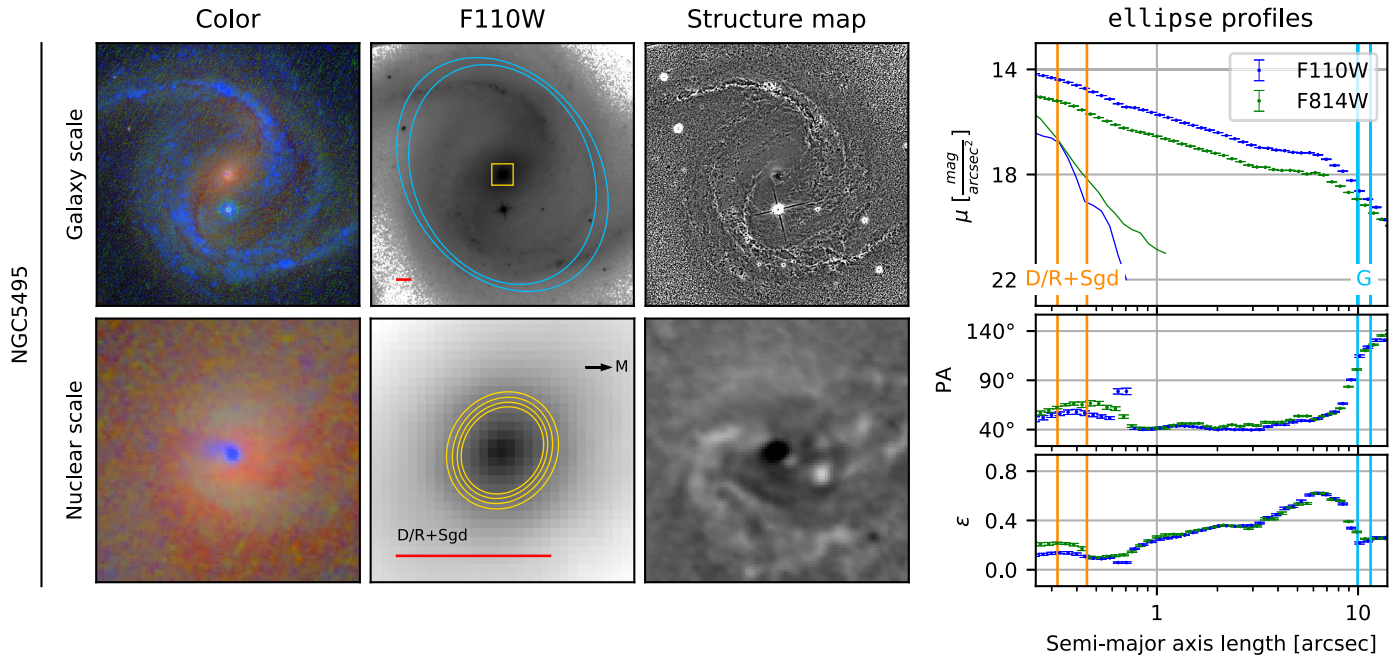
Figure 10. Images and `ellipse` fits of NGC 5495. The order of images and plots, as well as the meaning of symbols and designations, are the same as in Figure 1.

Appendix A
Images, Structure Maps, and `ellipse` Profiles of the Galaxies

A.1. ESO 558−G009

ESO 558−G009 (Figure 7) is a highly inclined Sb galaxy (Lauberts 1982) 115 Mpc from Earth (luminosity distance, Mould et al. 2000). Two counterclockwise-wound spiral arms are visible in the F110W image. The central regions of ESO 558−G009 are obscured by a pronounced dust lane. We identify a nuclear region with radius ∼0.4 arcsec (200 pc). Its main identifying features in the `ellipse` profiles are a plateau in eccentricity in F110W between 0.3 and 0.5 arcsec, a break in surface brightness at its inner edge (0.3 arcsec), and

a maximum in F814W PA profile at 0.4 arcsec. The structure map reveals a dust structure associated with these features in `ellipse` fits, which supports the distinct character of this region. However, no clear morphological type can be assigned in this case.

A.2. J0437+2456

The luminosity distance to J0437+2456 (Figure 8) is ∼70 Mpc (Pesce et al. 2015). It is a faint, probably Sb-type galaxy with no Hubble Type in the literature. The inclination is quite high, ∼60°. Two counterclockwise-wound spiral arms are clearly visible, extending from a "boxy" (peanut-shaped) bulge on larger scales. The central region of J0437+2456 is marked by a flattened maximum in PA profile at ∼0.4 arcsec (110 pc), corresponding to a flat region in eccentricity. This region corresponds to an elliptical structure in the structure map and seems consistent with a small-scale bulge.

A.3. Mrk 1029

Mrk 1029 (Figure 1) is an Irr/S galaxy (first position data: Kojoian et al. 1981; morphological identification as spiral: 2MASS, Skrutskie et al. 2006) located 124 Mpc from Earth (luminosity distance, Mould et al. 2000). It has a counter-clockwise-wound spiral structure (arms winding counterclock-wise from inside out) consisting of two faint kpc-scale spiral arms. The galaxy seems to be moderately inclined. As the nuclear region in the galaxy, we identify a ∼0.4 arcsec (220 pc) structure, where the PA profile flattens and the ellipticity forms a distinct region with an inward increase. A feature in the surface brightness profile can also be identified in both the F814W and F110W filters. Spatially, the selected nuclear region follows a dust structure clearly visible on the structure map. An interesting feature of this galaxy is the absence of any structure in the dust on scales larger than ∼0.5 kpc.
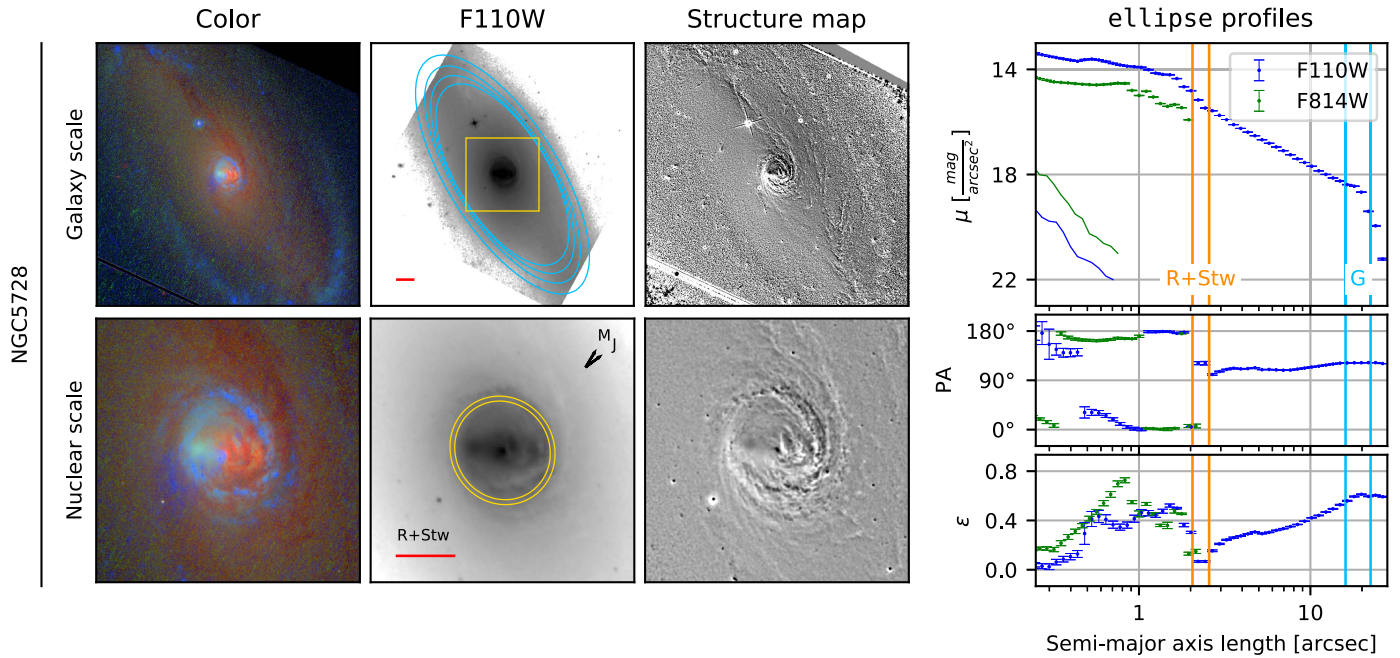
Figure 11. Images and `ellipse` fits of NGC 5728. The order of images and plots, as well as the meaning of symbols and designations, are the same as in Figure 1.

A.4. Mrk 1210

We classify Mrk 1210 (Figure 9; the Phoenix Galaxy) as a face-on Sc galaxy. It has been discovered to be a Seyfert galaxy by Balzano (1983), and its luminosity distance is 59.5 Mpc (Mould et al. 2000). A jet PA has been measured by Xanthopoulos et al. (2010) to be 125° at 50 pc. The spiral structure is wound clockwise with two arms clearly visible. We identify a ~0.6 arcsec (170 pc) nuclear feature characterized by a flattening in the PA profile and a maximum in ellipticity. No dust features seem to be associated with it in the galaxy's structure map. However, spiral structure appears to be visible around it, so we find it likely to be either a disk or a ring. We note that the maser interpretation of the radio features seen in Mrk 1210 is less certain than in the other sources.

A.5. NGC 5495

NGC 5495 (Figure 10) is a barred Sc galaxy (adapted from de Vaucouleurs et al. 1991) with a luminosity distance of 97.5 Mpc (Mould et al. 2000). It is moderately inclined and hosts a large bar with two bright, counterclockwise-wound spiral arms. The nuclear region's radius is ~0.4 arcsec (170 pc), as indicated by flattened maxima in PA and ellipticity profiles. A bar or spiral structure appears to be visible in dust within this nuclear region, so we classify it as either a disk or a ring. A two-arm grand-design nuclear spiral is also present (see discussion in Section 4).

A.6. NGC 5728

NGC 5728 (Figure 11) is a barred Sa galaxy (de Vaucouleurs et al. 1991), exhibiting Sy1.9 activity (Véron-Cetty & Véron 2006). Its luminosity distance is 41.9 Mpc (Mould et al. 2000). It is moderately inclined ($i \sim 65°$) and contains a large bar, from which two counterclockwise-wound spiral arms extend. The PA of a jet at 900 pc has been measured by Schommer et al. (1988) to be 307°. We note that the maser interpretation of the radio features seen in NGC 5728 is less certain than in the other sources.

In the case of NGC 5728, we identify a nuclear ring ~2 arcsec (460 pc) in radius (described in detail by Schommer et al. 1988 and Wilson et al. 1993) as the nuclear region. The `ellipse` profile shows a discontinuity in PA and near-zero ellipticity at this scale. This is not the smallest resolved structure in the galaxy images—more features can clearly be seen inside it. However, it appears to be the smallest structure in the nucleus with a clear interpretation. The angular momentum of the nuclear ring is pointed toward 121° or 301°. The nuclear ring is inclined at ±21° with regard to the Celestial Sphere. Note that the `ellipse` data allow for four possible angular momentum orientations for the ring (see Section 3.5). Outside the nuclear ring, a tightly wound nuclear spiral can be seen. While it is undetected in the `ellipse` profiles, it is obvious in the structure map, demonstrating the advantage of using multiple tools to interpret the features in galactic nuclei. As noted previously, more structure can be seen inside the nuclear ring of NGC 5728. While in the F110W image it closely resembles a bar along the east–west line connected with the nuclear ring, on the dust structure map it looks like a flocculent spiral with a smoother patch at the eastern side in the blue filter, seen as a cone-like region in the color image. This feature has been identified by Schommer et al. (1988) and later confirmed by Wilson et al. (1993) to be an AGN ionization cone. The emission from the NLR overwhelms any dust structure in the same part of the image as the cone. This is why the inner nuclear spiral can only be seen on the western side of the structure map. Interestingly, the ionization cone corresponds to a region with positive radial velocity with respect to systemic, as shown using Hα spectrometry by Schommer et al. (1988; see their Figure 9). If the ionization region corresponds to an outflow (as we would expect), it would have to be directed away from us. However, as argued by Wilson et al. (1993), the true orientation of this main ionization cone (and its counterpart in the SW direction) is uncertain. Schommer et al. (1988) also report a jet in
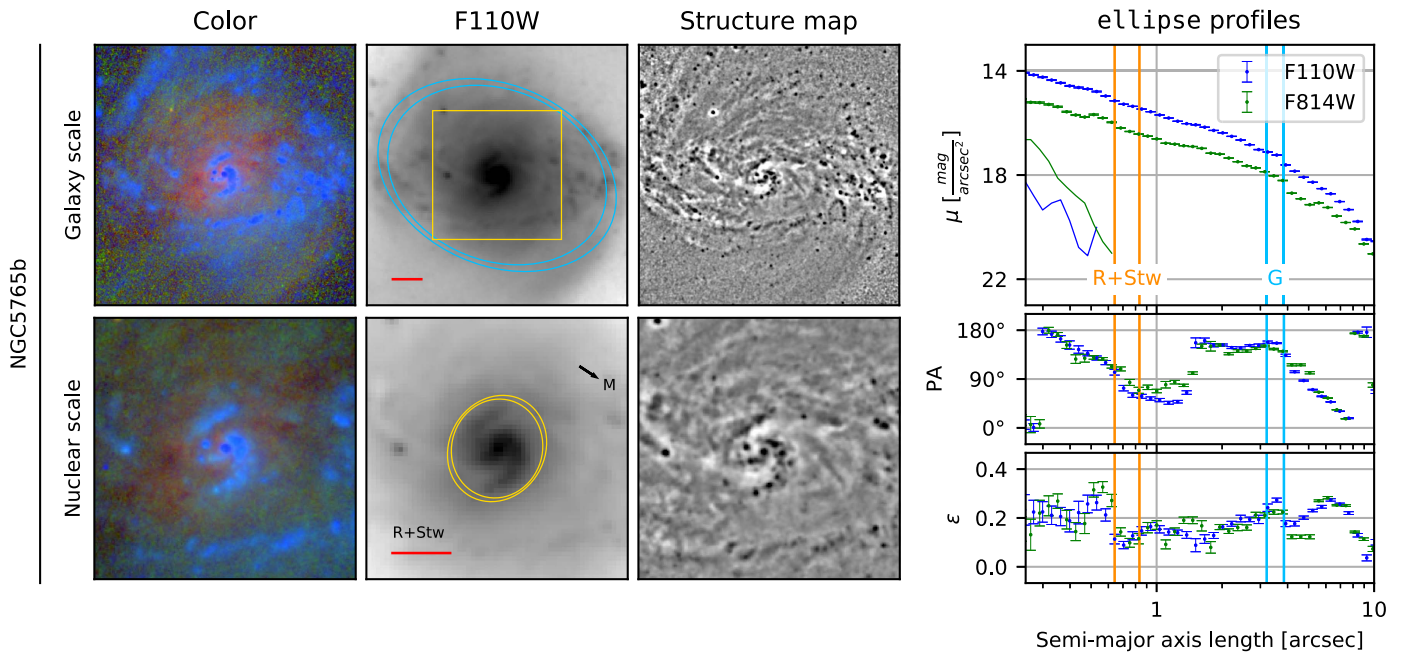
Figure 12. Images and `ellipse` fits of NGC 5765b. The order of images and plots, as well as the meaning of symbols and designations, are the same as in Figure 1.
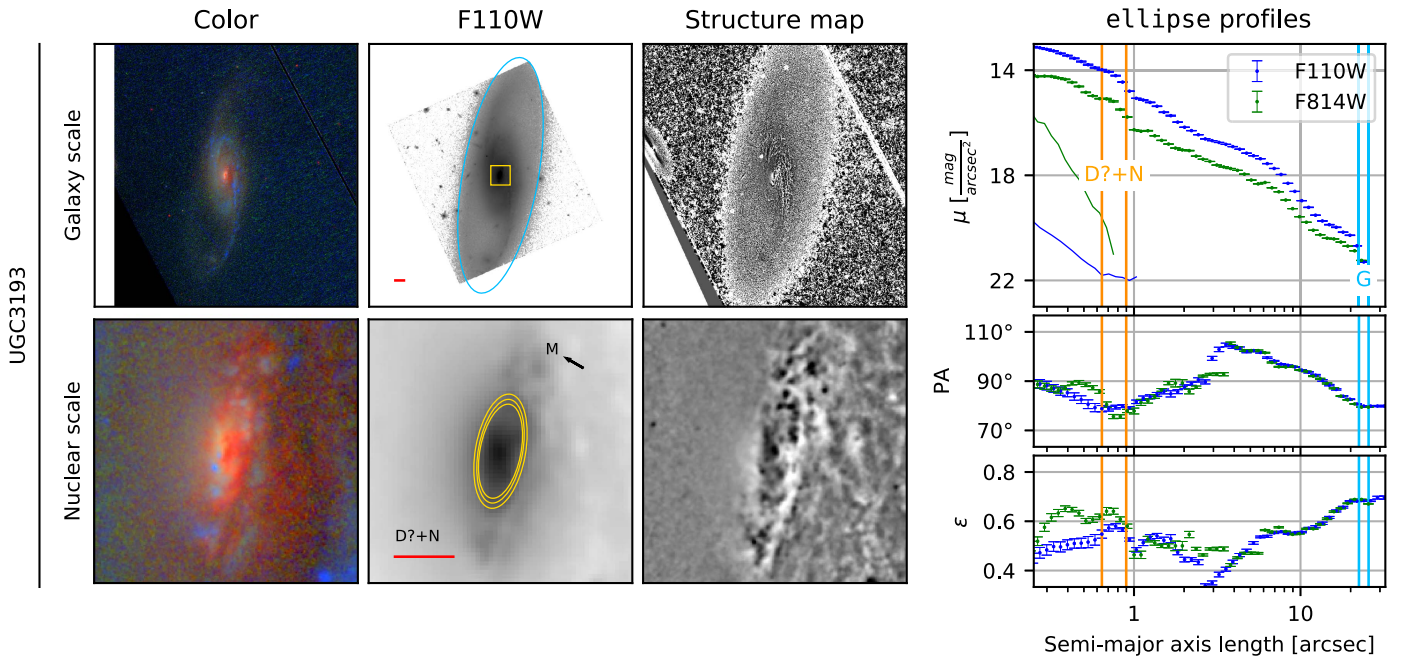

Figure 13. Images and `ellipse` fits of UGC 3193. The order of images and plots is the same as in Figure 1. In the nuclear-scale F110W image of UGC 3193, the red bar is 0.5 kpc long in projected distance. The meaning of the remaining symbols and designations is the same as in Figure 1.

NGC 5728. It extends in the opposite direction from the large (SE) ionization cone, and its projection is aligned with the projection of the megamaser disk's angular momentum.

A.7. NGC 5765b

NGC 5765b (Figure 12) is an Sab galaxy located 126.3 Mpc from the Earth (Gao et al. 2016, angular diameter distance). It constitutes a pair with NGC 5765a, and its activity has been classified as Sy2 (Shirazi & Brinchmann 2012). The galaxy contains two large-scale rings ∼3.5 and ∼1.5 arcsec in radius

(see Figure 12). Spiral structure is seen both within and outside each of the rings; it is wound clockwise with pitch angles changing between the rings (as can be seen in PA `ellipse` profiles in Figure 12). Beyond the outer large-scale ring, the galaxy starts to exhibit signs of interaction with NGC 5765a. As the nuclear region, we identify a small-scale ring with radius of ∼0.7 arcsec (∼450 pc). A nuclear spiral is clearly visible around it. While in the F110W image the spiral inside the nuclear ring appears grand-design, the structure map reveals rich structure associated with it. We therefore classify it as a tightly wound spiral.
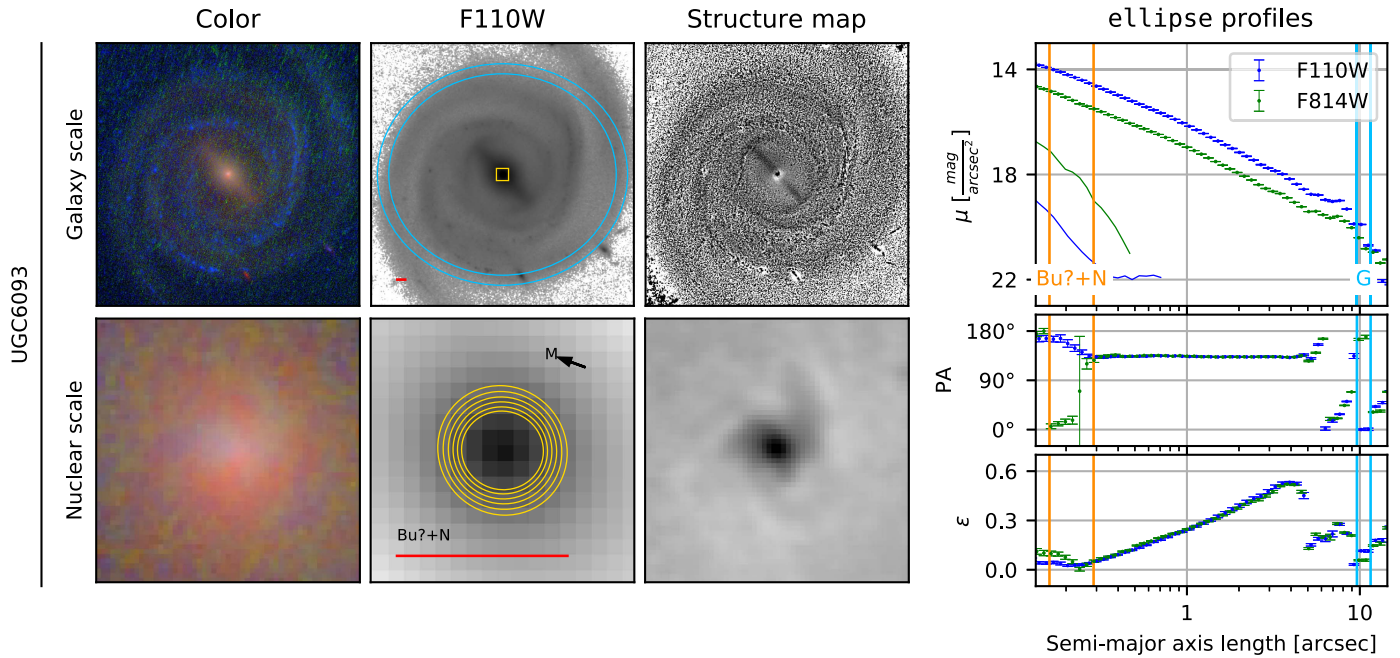
Figure 14. Images and `ellipse` fits of UGC 6093. The order of images and plots, as well as the meaning of symbols and designations, are the same as in Figure 1.

A.8. UGC 3193

The galaxy morphology for UGC 3193 (Figure 13) is barred-Sab (de Vaucouleurs et al. 1991), and it is located 61.3 Mpc from Earth (Mould et al. 2000), seen close to edge-on. It is a member of a galaxy group. The spiral structure is clear, with two large-scale arms wound clockwise. A large-scale bar is identified in the `ellipse` profiles at $\sim 3''$. The nuclear region we identify shows a clear maximum in ellipticity profile at $r \sim 0.8$ arcsec (220 pc), corresponding to a minimum in PA. A distinct feature is also visible in the surface brightness `ellipse` profile. While there appears to be a dust structure at the selected region, it does not straightforwardly point at its morphological type. However, as the `ellipse` fits contain prominent signatures of the flattened character of that structure, we treat it as a possible disk feature. On smaller scales, the `ellipse` profiles point at the existence of a bulge (minimum of ellipticity at ~ 0.5 arcsec) and a small-scale bar (maximum of ellipticity at ~ 0.4 arcsec), visible as a dark lane across the chosen nuclear region in the structure map.

A.9. UGC 6093

UGC 6093 (Figure 14) is a barred-Sbc (de Vaucouleurs et al. 1991) with a luminosity distance of 158 Mpc (Mould et al. 2000). The large-scale structure consists of a central bulge and a bar connected to a large-scale ring, from which two large spiral arms extend counterclockwise. As the central structure we identify a region with a minimum in the F814W ellipticity profile and a change in PA opposite for F110W and F814W at ~ 0.2 arcsec (150 pc). No additional structure is visible in the brightness profile. While there appears to be a near-circular feature visible in the structure map, it is nearing on the PSF scale, so we classify this region as an uncertain bulge. In addition, a dim two-arm grand-design spiral may be distinguished outside this region in the structure map. It is, however, too uncertain to be included in the region's classification.

Appendix B
Structure Classification—Dependence on Galaxy Distance and Scale of the Nuclear Region

B.1. Dependence on Galaxy Distance

We assess the robustness of our classification by analyzing how the classes depend on distance to the host galaxy (and, correspondingly, the image resolution). The distribution of each class as a function of host galaxy distance is shown in Figure 15. The histograms on the left depict the nuclear region by class. Disky and ring-like nuclear structures are best visible for close galaxies due to superior resolution, allowing us to resolve features associated with the flatness of a structure, such as nuclear spirals. Further away, more nuclear regions are classified as "chaotic"—some of which are possibly disky structures that are too distant to allow certain classification—or "possible bulges." Note that due to our simplistic approach to their identification, bulge classification is treated by us with caution. To properly decompose bulges from nuclear disks requires 2D image fitting (e.g., Läsker et al. 2016), which is beyond the scope of this work. The main reason to include nuclear bulges in our analysis is to avoid measurement of orientation of non-disky nuclear regions (see Section 3.5)—a goal that should be achieved even if some of the Bu? objects are misclassified. The dependencies listed show that there are biases in our classification due to the decrease in available image resolution with distance, as signaled by the "unsure" (question marks) or "chaotic" (Ch) categories. Similar reasoning holds true for the nuclear spirals, which we appear to assign as "N" if unresolved (see the right panel of Figure 15).

In the left part of Figure 15 one can note a division between $D \lesssim 80$ Mpc, where almost all the classifications are robust, and $D \gtrsim 80$ Mpc, with a considerable fraction of either unsure (marked with "?") or chaotic (Ch) nuclear regions. We therefore conclude that our classifications for galaxies less than 80 Mpc away are not affected by angular resolution bias and can be specifically trusted. In addition, we see that while for galaxies beyond $D \sim 60$ Mpc our chosen nuclear regions
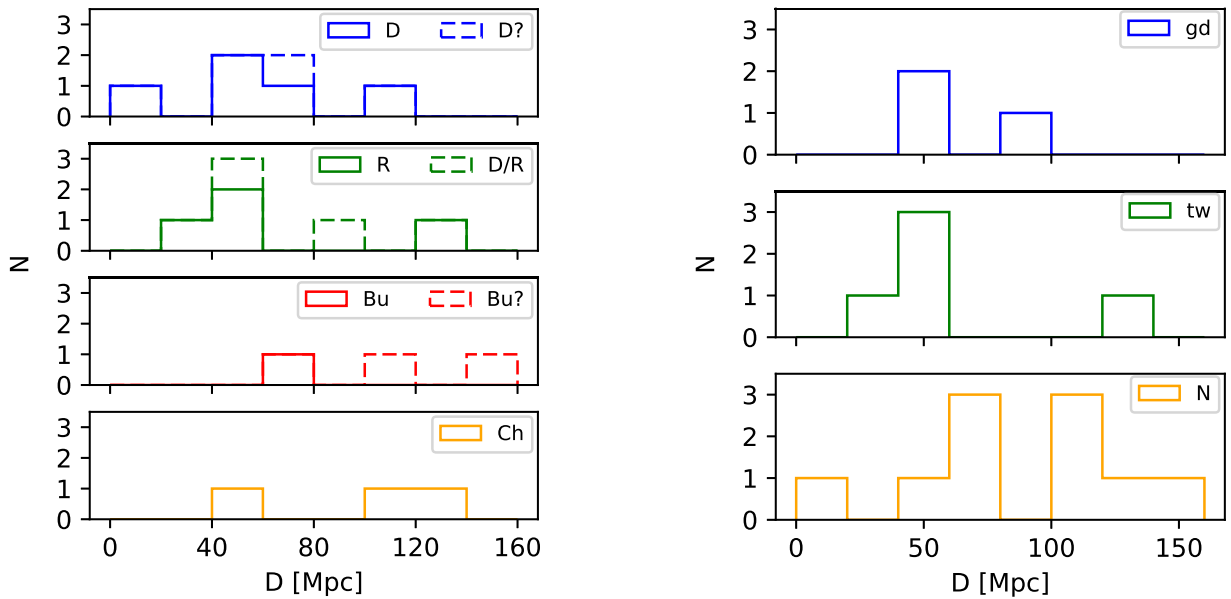
Figure 15. Left: distribution of nuclear region classes as a function of angular diameter distance to the host galaxy. Notation: D—disk, R—ring, Bu—bulge, Ch—chaotic nuclear dust structure; "?" denotes uncertain classification. Right: distribution of nuclear spiral classes as a function of angular diameter distance to the host galaxy. Possible nuclear spiral classes: gd—grand-design nuclear spiral, tw—tightly wound nuclear spiral, N—no nuclear spiral visible.
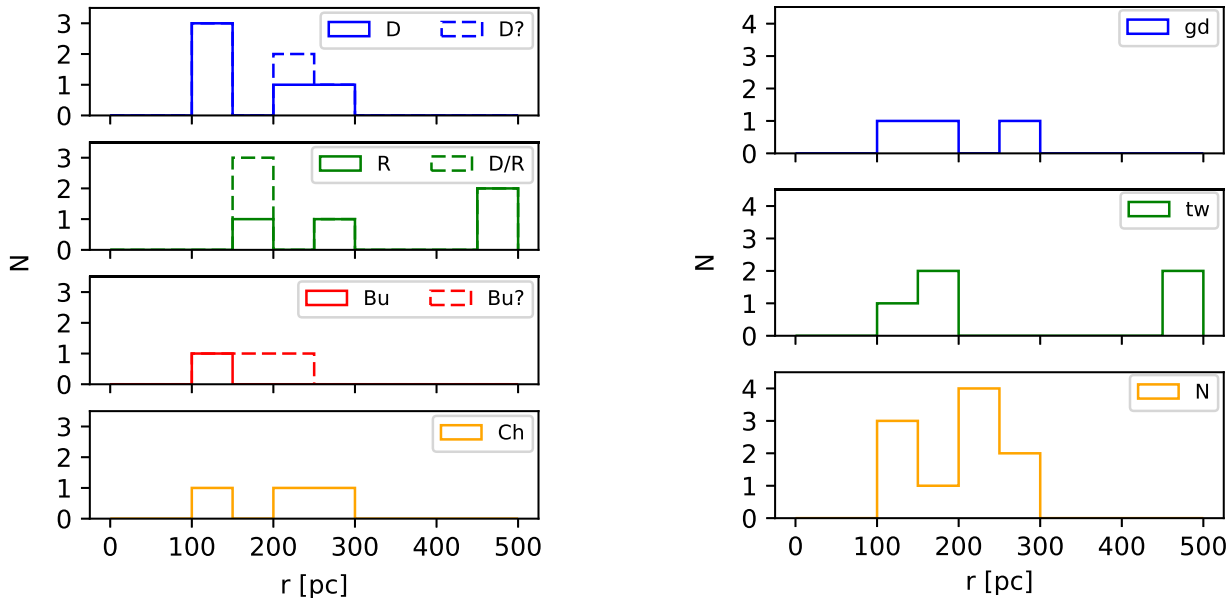

Figure 16. Left: distribution of nuclear region classes as a function of the region scale. Notation: D—disk, R—ring, Bu—bulge, Ch—chaotic nuclear dust structure; "?" denotes uncertain classification. Right: distribution of nuclear spiral classes as a function of the scale of the corresponding nuclear region. Nuclear spiral classes: gd—grand-design, tw—tightly wound, N—no nuclear spiral visible.

assume different morphologies, almost all of them are disk-like (either of D or R type) below that limiting distance.

In the right-side histograms of Figure 15, the distribution in host distance for the classes of nuclear spirals is shown. Grand-design (gd) structures are easily recognizable in the entire range of distances, and it appears unlikely that any of the "N" (no nuclear spiral visible) sources are in fact unresolved "gd"s (grand-design nuclear spirals). While the "N" sources in further galaxies must in part be unresolved "tw"s, their flattened distribution with distance suggests that there are intrinsically chaotic dust structures in our sample as well.

B.2. Dependence on Scale of the Nuclear Region

The left-side histograms of Figure 16 show the distribution of different classes of nuclear regions as a function of the physical scale of the region. We observe a transition between a mixture of nuclear structure types at 150–300 pc to almost exclusively disky environments at smaller scales. We observe disk-like nuclear regions in virtually *all* of our galaxies closer than ∼60 Mpc (see Figure 15). Perhaps in some of the more distant sources similar features remain undetected at larger scales available to us. Distributions of nuclear spiral types with

Table 4
Results of the KS Tests for Nuclear Regions Larger Than 0.5 arcsec

Species		Angle	Limit	N	KS-stat	p-value
(1)	(2)	(3)	(4)	(5)	(6)	(7)
Gal	Nuc	ΔPA	30°	10	0.30	0.27
Gal	Nuc	ΔPA	90°	10	0.42	0.04
Gal	Nuc(S)	ΔPA	30°	5	0.50	0.11
Gal	Nuc(S)	ΔPA	90°	5	0.32	0.59
Gal	Nuc(L)	ΔPA	30°	5	0.43	0.23
Gal	Nuc(L)	ΔPA	90°	5	0.64	0.02
Nuc	Mas	ΔPA	90°	10	0.42	0.04
Nuc(S)	Mas	ΔPA	90°	5	0.32	0.59
Nuc(L)	Mas	ΔPA	90°	5	0.69	0.01
Nuc	Mas	3D	90°	10	0.31	0.24
Nuc(S)	Mas	3D	90°	5	0.32	0.61
Nuc(L)	Mas	3D	90°	5	0.31	0.64
Gal*	Mas	ΔPA	90°	10	0.30	0.27
Gal*	Mas	3D	180°	10	0.30	0.26

Note. Results of one-sample KS tests for a sample limited to galaxies with nuclear regions larger than 0.5 arcsec. The division between small and large nuclear regions remains at 200 pc. For a description of KS tests, see Section 5.1. The meaning of columns and notation is the same as in Table 3.

scale seem relatively flat, suggesting that the type of such structure does not depend on the physical scale of the region.

As noted in Section 3.3, all of our nuclear structures were identified at sizes of at least 0.3 arcsec. To make sure that such limiting angular size is sufficient and resolution effects do not affect the results presented in Sections 4 and 5, we have re-derived these results with a more restrictive limit on angular size of a nuclear region of 0.5 arcsec. As a result, we limited our sample to 10 of the 18 galaxies. We used the same limit between small and large nuclear regions of 200 pc to divide the re-derived sample. Due to different distances to galaxies, the sizes of these sub-samples were still comparable, with five small and five large nuclear regions, respectively. As can be seen in results of KS tests presented in Table 4, our conclusions (see Sections 4 and 5) remained mostly unchanged (cf. Table 3). We note two differences in comparison with Table 3. First, in this limited sample we cannot rule out that both small and large nuclear regions align with the kpc-scale galaxy, although the p-value for random orientation of small nuclear regions is still larger than that for their being aligned (see discussion in Section 5.1.2). Second, in this test the distribution of relative PAs between large nuclear regions and the masing disks is seemingly inconsistent with random (p-value = 0.01), while the small nuclear regions remain randomly oriented with regard to their megamasers. We find this unlikely to be a physical effect, as the information about maser orientation would have to "jump over" the small nuclear regions. Moreover, the results of KS tests using the 3D angles between angular momenta of large nuclear regions and masing disks remain consistent with their random relative orientation (with p-value even improving from 0.42 in the initial sample [see Table 3] to 0.64 in the limited one [Table 4]). Since these results utilize additional information, the inclination of nuclear regions, we regard them as more trustworthy than the PAs alone. We conclude that even in the sample limited to 0.5 arcsec, both small and large nuclear regions are consistent with being fully randomly oriented with respect to their masing disks.

References

Anglés-Alcázar, D., Davé, R., Faucher-Giguère, C.-A., Özel, F., & Hopkins, P. F. 2017, MNRAS, 464, 2840
Balzano, V. A. 1983, ApJ, 268, 602
Barnes, J. E., & Hernquist, L. 1996, ApJ, 471, 115
Becker, R. H., White, R. L., Helfand, D. J., Greeg, M. D., & Perley, R. A. 1994, BAAS, 26, 1317
Bertola, F., Bettoni, D., Rusconi, L., & Sedmak, G. 1984, AJ, 89, 356
Binney, J., & Tremaine, S. 2008, Galactic Dynamics (2nd ed.; Princeton, NJ: Princeton Univ. Press)
Bournaud, F., Elmegreen, B. G., & Elmegreen, D. M. 2007, ApJ, 670, 237
Braatz, J. A., Wilson, A. S., & Henkel, C. 1997, ApJS, 110, 321
Buta, R. 1986, ApJS, 61, 609
Canalizo, G., & Stockton, A. 2001, ApJ, 555, 719
Cavaliere, A., & Vittorini, V. 2000, ApJ, 543, 599
Cisternas, M., Jahnke, K., Inskip, K. J., et al. 2011, ApJ, 726, 57
Combes, F., García-Burillo, S., Casasola, V., et al. 2014, A&A, 565, A97
Comerford, J. M., & Greene, J. E. 2014, ApJ, 789, 112
Cooke, A. J., Baldwin, J. A., Ferland, G. J., Netzer, H., & Wilson, A. S. 2000, ApJS, 129, 517
Davies, R. I., Maciejewski, W., Hicks, E. K. S., et al. 2009, ApJ, 702, 114
Davies, R. I., Maciejewski, W., Hicks, E. K. S., et al. 2014, ApJ, 792, 101
De Rosa, G., Venemans, B. P., Decarli, R., et al. 2014, ApJ, 790, 145
de Vaucouleurs, G., de Vaucouleurs, A., Corwin, H. G., Jr., et al. 1991, Third Reference Catalogue of Bright Galaxies, Vol. I, II, III (New York: Springer)
Diniz, M. R., Riffel, R. A., Storchi-Bergmann, T., & Winge, C. 2015, MNRAS, 453, 1727
Ellison, S. L., Patton, D. R., Mendel, J. T., & Scudder, J. M. 2011, MNRAS, 418, 2043
Englmaier, P., & Shlosman, I. 2000, ApJ, 528, 677
Erwin, P., & Sparke, L. S. 2003, ApJS, 146, 299
Escala, A. 2007, ApJ, 671, 1264
Falcke, H., Wilson, A. S., & Simpson, C. 1998, ApJ, 502, 199
Fischer, T. C., Crenshaw, D. M., Kraemer, S. B., & Schmitt, H. R. 2013, ApJS, 209, 1
Gallimore, J. F., Axon, D. J., O'Dea, C. P., Baum, S. A., & Pedlar, A. 2006, AJ, 132, 546
Gammie, C. F., Goodman, J., & Ogilvie, G. I. 2000, MNRAS, 318, 1005
Gao, F., Braatz, J. A., Reid, M. J., et al. 2016, ApJ, 817, 128
Gao, F., Braatz, J. A., Reid, M. J., et al. 2017, ApJ, 834, 52
García-Burillo, S., Combes, F., Usero, A., et al. 2014, A&A, 567, A125
Gatti, M., Lamastra, A., Menci, N., Bongiorno, A., & Fiore, F. 2015, A&A, 576, A32
Genzel, R., Burkert, A., Bouché, N., et al. 2008, ApJ, 687, 59
Goodman, J. 2003, MNRAS, 339, 937
Greene, J. E., Peng, C. Y., Kim, M., et al. 2010, ApJ, 721, 26
Greene, J. E., Seth, A., den Brok, M., et al. 2013, ApJ, 771, 121
Greene, J. E., Seth, A., Kim, M., et al. 2016, ApJL, 826, L32
Greene, J. E., Seth, A., Lyubenova, M., et al. 2014, ApJ, 788, 145
Greenhill, L. J., Booth, R. S., Ellingsen, S. P., et al. 2003, ApJ, 590, 162
Greenhill, L. J., Moran, J. M., Reid, M. J., et al. 1990, ApJ, 364, 513
Haan, S., Schinnerer, E., Emsellem, E., et al. 2009, ApJ, 692, 1623
Heckman, T. M., Balick, B., & Sullivan, W. T., III 1978, ApJ, 224, 745
Hernquist, L. 1989, Natur, 340, 687
Hernquist, L., & Mihos, J. C. 1995, ApJ, 448, 41
Herrnstein, J. R., Moran, J. M., Greenhill, L. J., & Trotter, A. S. 2005, ApJ, 629, 719
Hicks, E. K. S., Davies, R. I., Maciejewski, W., et al. 2013, ApJ, 768, 107
Hopkins, P. F., & Hernquist, L. 2009, ApJ, 694, 599
Hopkins, P. F., Hernquist, L., Hayward, C. C., & Narayanan, D. 2012, MNRAS, 425, 1121
Hopkins, P. F., & Quataert, E. 2010, MNRAS, 407, 1529
Hopkins, P. F., & Quataert, E. 2011, MNRAS, 415, 1027
Hubble, E. P. 1929, ApJ, 69
Izumi, T., Kawakatu, N., & Kohno, K. 2016, ApJ, 827, 81
Jedrzejewski, R. I. 1987, MNRAS, 226, 747
Jungwiert, B., Combes, F., & Axon, D. J. 1997, A&AS, 125 arXiv:astro-ph/9705175
Kim, W.-T., Seo, W.-Y., & Kim, Y. 2012, ApJ, 758, 14
Kinney, A. L., Schmitt, H. R., Clarke, C. J., et al. 2000, ApJ, 537, 152
Kocevski, D. D., Faber, S. M., Mozena, M., et al. 2012, ApJ, 744, 148
Kojoian, G., Elliott, R., & Bicay, M. D. 1981, AJ, 86, 816

Kondratko, P. T., Greenhill, L. J., & Moran, J. M. 2008, ApJ, 678, 87
Kormendy, J., & Ho, L. C. 2013, ARA&A, 51, 511
Kormendy, J., & Kennicutt, R. C., Jr. 2004, ARA&A, 42, 603
Kuo, C. Y., Braatz, J. A., Condon, J. J., et al. 2011, ApJ, 727, 20
Läsker, R., Greene, J. E., Seth, A., et al. 2016, ApJ, 825, 3
Lauberts, A. 1982, ESO/Uppsala Survey of the ESO(B) Atlas (Munich: European Southern Observatory)
Lo, K. Y. 2005, ARA&A, 43, 625
Lucy, L. B. 1974, AJ, 79, 745
Maciejewski, W., Teuben, P. J., Sparke, L. S., & Stone, J. M. 2002, MNRAS, 329, 502
Maiolino, R., Alonso-Herrero, A., Anders, S., et al. 2000, ApJ, 531, 219
Maloney, P. R., Begelman, M. C., & Pringle, J. E. 1996, ApJ, 472, 582
Márquez, I., Durret, F., Masegosa, J., et al. 2000, A&A, 360, 431
Martini, P. 2004, in Penetrating Bars Through Masks of Cosmic Dust, Vol. 319, ed. D. L. Block et al. (New York: Springer), 213
Martini, P., Regan, M. W., Mulchaey, J. S., & Pogge, R. W. 2003, ApJ, 589, 774
Middleton, M. J., Parker, M. L., Reynolds, C. S., Fabian, A. C., & Lohfink, A. M. 2016, MNRAS, 457, 1568
Morganti, R., de Zeeuw, P. T., Oosterloo, T. A., et al. 2006, MNRAS, 371, 157
Mortlock, D. J., Warren, S. J., Venemans, B. P., et al. 2011, Natur, 474, 616
Mould, J. R., Huchra, J. P., Freedman, W. L., et al. 2000, ApJ, 529, 786
Mundell, C. G., Ferruit, P., Nagar, N., & Wilson, A. S. 2009, ApJ, 703, 802
Nagar, N. M., & Wilson, A. S. 1999, ApJ, 516, 97
Nair, P. B., & Abraham, R. G. 2010, ApJS, 186, 427
Neufeld, D. A., & Maloney, P. R. 1995, ApJL, 447, L17
Noguchi, M. 1998, Natur, 392, 253
Peeples, M. S., & Martini, P. 2006, ApJ, 652, 1097
Pesce, D. W., Braatz, J. A., Condon, J. J., et al. 2015, ApJ, 810, 65
Pogge, R. W., & Martini, P. 2002, ApJ, 569, 624
Pringle, J. E. 1997, MNRAS, 292, 136
Rees, M. J. 1984, ARA&A, 22, 471
Regan, M. W., & Mulchaey, J. S. 1999, AJ, 117, 2676
Richardson, W. H. 1972, JOSA, 62, 55
Riffel, R. A., Storchi-Bergmann, T., & Winge, C. 2013, MNRAS, 430, 2249

Sarzi, M., Falcón-Barroso, J., Davies, R. L., et al. 2006, MNRAS, 366, 1151
Schmitt, H. R., Pringle, J. E., Clarke, C. J., & Kinney, A. L. 2002, ApJ, 575, 150
Schmitt, H. R., Ulvestad, J. S., Antonucci, R. R. J., & Kinney, A. L. 2001, ApJS, 132, 199
Schommer, R. A., Caldwell, N., Wilson, A. S., et al. 1988, ApJ, 324, 154
Schulz, H., & Henkel, C. 2003, A&A, 400, 41
Sharp, N. A., & Keel, W. C. 1985, AJ, 90, 469
Shibuya, T., Ouchi, M., Kubo, M., & Harikane, Y. 2016, ApJ, 821, 72
Shirazi, M., & Brinchmann, J. 2012, MNRAS, 421, 1043
Shlosman, I., & Begelman, M. C. 1989, ApJ, 341, 685
Shlosman, I., Frank, J., & Begelman, M. C. 1989, Natur, 338, 45
Simões Lopes, R. D., Storchi-Bergmann, T., de Fátima Saraiva, M., & Martini, P. 2007, ApJ, 655, 718
Skrutskie, M. F., Cutri, R. M., Stiening, R., et al. 2006, AJ, 131, 1163
Sun, A.-L., Greene, J. E., Impellizzeri, C. M. V., et al. 2013, ApJ, 778, 47
Treister, E., Schawinski, K., Urry, C. M., & Simmons, B. D. 2012, ApJL, 758, L39
Ulvestad, J. S., & Wilson, A. S. 1984, ApJ, 278, 544
Väisänen, P., Ryder, S., Mattila, S., & Kotilainen, J. 2008, ApJL, 689, L37
van den Bosch, R. C. E., Gebhardt, K., Gültekin, K., Yıldırım, A., & Walsh, J. L. 2015, ApJS, 218, 10
van den Bosch, R. C. E., Greene, J. E., Braatz, J. A., Constantin, A., & Kuo, C.-Y. 2016, ApJ, 819, 11
Venemans, B. P., Findlay, J. R., Sutherland, W. J., et al. 2013, ApJ, 779, 24
Véron-Cetty, M.-P., & Véron, P. 2006, A&A, 455, 773
Villforth, C., Hamann, F., Rosario, D. J., et al. 2014, MNRAS, 439, 3342
Wilson, A. S., Braatz, J. A., Heckman, T. M., Krolik, J. H., & Miley, G. K. 1993, ApJL, 419, L61
Xanthopoulos, E., Thean, A. H. C., Pedlar, A., & Richards, A. M. S. 2010, MNRAS, 404, 1966
Xilouris, E. M., & Papadakis, I. E. 2002, A&A, 387, 441
Yamauchi, A., Nakai, N., Ishihara, Y., Diamond, P., & Sato, N. 2012, PASJ, 64, 103